

# Model Simulations Unveil The Structure-Function-Dynamics Relationship of The Cerebellar Cortical Microcircuit

**Robin De Schepper**

University of Pavia

**Alice Geminiani**

University of Pavia

**Stefano Masoli**

University of Pavia <https://orcid.org/0000-0003-0660-9952>

**Martina Francesca Rizza**

University of Pavia

**Alberto Antonietti**

University of Pavia <https://orcid.org/0000-0003-0388-6321>

**Claudia Casellato**

University of Pavia

**Egidio D'Angelo** (✉ [dangelo@unipv.it](mailto:dangelo@unipv.it))

University of Pavia <https://orcid.org/0000-0002-6007-7187>

---

## Article

**Keywords:** computational modeling, structure-function relationship, cerebellum, neuronal, microcircuits, multi-compartmental neuron models

**Posted Date:** November 2nd, 2021

**DOI:** <https://doi.org/10.21203/rs.3.rs-886369/v1>

**License:** © ⓘ This work is licensed under a Creative Commons Attribution 4.0 International License.

[Read Full License](#)

**Additional Declarations:** There is **NO** Competing Interest.

---

**Version of Record:** A version of this preprint was published at Communications Biology on November 14th, 2022. See the published version at <https://doi.org/10.1038/s42003-022-04213-y>.

# 1 Model simulations unveil the structure-function-dynamics relationship of 2 the cerebellar cortical microcircuit

3 Robin De Schepper<sup>1</sup>, Alice Geminiani<sup>1</sup>, Stefano Masoli<sup>1</sup>, Martina Francesca Rizza<sup>1</sup>, Alberto Antonietti<sup>1</sup>,  
4 Claudia Casellato<sup>1,#</sup>, Egidio D'Angelo<sup>1,2,#</sup>

5 <sup>1</sup>*Department of Brain and Behavioral Sciences, University of Pavia, Pavia, Italy.*

6 <sup>2</sup>*IRCCS Mondino Foundation, Brain Connectivity Center, Pavia, Italy.*

7 # Co-last and corresponding authors

8  
9 **Running title:** Realistic cerebellar cortex model

10 **Keywords:** computational modeling, structure-function relationship, cerebellum, neuronal  
11 microcircuits, multi-compartmental neuron models

## 12 13 1 Abstract

14 The cerebellar network is renowned for its regular architecture that has inspired foundational  
15 computational theories. However, the relationship between circuit structure, function and dynamics  
16 remained elusive. To tackle the issue, we have developed an advanced computational modeling  
17 framework that allowed us to reconstruct and simulate the structure and function of the mouse cerebellar  
18 cortex using morphologically realistic multi-compartmental neuron models. The cerebellar connectome  
19 was generated through appropriate connection rules, unifying a collection of scattered experimental  
20 data into a coherent construct and providing a new model-based ground-truth about circuit organization.  
21 Naturalistic background and sensory-burst stimulation were then used for functional validation against  
22 recordings *in vivo*, monitoring the impact of cellular mechanisms on signal propagation and spatio-  
23 temporal processing. Our simulations show, for the first time, how mossy fibers entrain the local  
24 neuronal microcircuit boosting the formation of columns of activity travelling from the granular to the  
25 molecular layer providing a new resource for the investigation of cerebellar computation.

## 26 27 2 Introduction

28 The relationship between structure, function and dynamics in brain circuits is still poorly  
29 understood posing a formidable challenge to neuroscience <sup>1</sup>. The core of the issue is how to deal with  
30 the distribution and causality of neural processing across multiple spatio-temporal scales. While  
31 experimental measurements remain essential, they can now be supported and complemented by realistic  
32 computational models. In principle, such models could take into account multi-modal datasets  
33 representing morphology, connectivity and activity of different cell populations and make it possible to  
34 simulate the propagation of microscopic phenomena into large-scale network dynamics <sup>2-4</sup>. These  
35 models can incorporate a broad range of biological data becoming highly constrained and providing the

36 best proxies of the corresponding natural circuits. Eventually, once properly configured and validated,  
37 these models can generate their own ground-truth by binding the many parameters, provided by  
38 independent measurements and intrinsically prone to experimental error, into a coherent construct, and  
39 can be used to test various functional hypotheses <sup>5</sup> using specific simulations platforms, like NEURON  
40 <sup>6</sup> and NEST <sup>7</sup>. There are several examples of advanced computational models that have been mostly  
41 developed to simulate activities in the cerebral cortex <sup>8-10</sup>. Here we have developed a specific simulator,  
42 the Brain Scaffold Builder (BSB), to cope with the organization of the cerebellar network.

43 The cerebellar cortical microcircuit has inspired foundational theories on brain functioning <sup>11</sup> but  
44 still challenges realistic computational modeling <sup>12</sup>. Previous network models using ionic conductance-  
45 based neurons have been developed only for the granular layer <sup>13,14</sup>. The only model encompassing the  
46 granular and molecular layer altogether made use of single-point neurons with a simplified  
47 representation of membrane excitability <sup>15</sup>. Although those models showed a remarkable predictive  
48 power against specific target parameters, their main limitation was that connectivity was set  
49 independently from neuronal morphology <sup>13-15</sup> preventing a direct link between microcircuit structure,  
50 function and dynamics. In the meanwhile, detailed computational models of the main cerebellar cortical  
51 neurons, which were based on morphological reconstructions embedding multiple membrane ionic  
52 channels and synaptic receptors, have been developed, tested and validated <sup>16-19</sup>. Thus, with the BSB,  
53 we have been able to generate the first computational model of the entire cerebellar cortical microcircuit  
54 including both the granular and molecular layer, in which multicompartmental neuron models were  
55 wired through a connectome defined by the anisotropy of dendritic and axonal processes through  
56 principled rules. The model allowed then to simulate network dynamics and validate it against  
57 naturalistic inputs <sup>20-22</sup>.

58 This work generates *de facto* a new model-based ground-truth for the cerebellar cortical  
59 microcircuit, predicting the weight that some connections should have to balance the internal activity.  
60 On the scale used here, there are two main emerging spatio-temporal dynamics. First, background  
61 mossy fiber bombardment induces coherent oscillations throughout the granular layer. Secondly,  
62 collimated mossy fibre bursts mimicking punctuate sensory stimulation generate dense clusters of  
63 granule cell activity that propagate vertically and invade the overlaying molecular layer. The emergence  
64 of these responses, which may represent the basis of local computation in the cerebellar microcircuit,  
65 anticipates properties revealed experimentally *in vivo* suggesting that the BSB cerebellar model will  
66 provide a valid resource for future cerebellar investigations.

67

68

### 69 3 Results

70

### 71 3.1 The Brain Scaffold Builder (BSB)

72 Cerebellar modelling using realistic morphologies poses specific problems, mostly related to the  
73 anisotropy and regular geometry of the network, that are not easily manageable with existing modeling  
74 tools<sup>8-10</sup> so that we developed a new simulation platform, the BSB. The BSB allowed to easily solve  
75 construction problems like the precise orientation of neuron process in the 3D space, the connectivity  
76 of neurons through prescribed rules dictated by anatomo-physiological measurements and the choice of  
77 a variety of intersection rules depending on network geometry. The BSB operated through a sequence  
78 of independent steps: network configuration, reconstruction and simulation (Fig. 1a). The network  
79 volume was defined first along with cell types, then the BSB proceeded with cell placement and  
80 connectivity, reconstructing the microcircuit network (Fig. 1b, c). Finally, the BSB was interfaced with  
81 the NEURON simulator and network activity was simulated and the results visualized. Details on BSB  
82 operations are given in the Methods and Supplemental Material.

### 84 3.2 Cerebellar network reconstruction

85 The BSB was applied to the mouse cerebellar cortical network, which has a geometrically  
86 organized architecture that has been suggested to imply its computational properties<sup>11,12</sup>. The  
87 reconstruction and simulation of a network volume of  $17.7 \cdot 10^{-3} \text{ mm}^3$  is reported, including the following  
88 cell and fiber types: mossy fiber (*mf*), glomerulus (*glom*), granule cell (*GrC*) with ascending axon (*aa*)  
89 and parallel fiber (*pf*), Golgi cell (*GoC*), Purkinje cell (*PC*), and molecular layer interneurons (*MLI*)  
90 comprising stellate cells (*SC*) and basket cells (*BC*).

#### 92 3.2.1 Neuron placement

93 The network elements summed up to 29'230 neurons (*GrC*, *GoC*, *PC*, *SC*, *BC*) plus 2'453 other  
94 elements (*mf*, *glom*), which were placed in the network volume according to anatomical data<sup>12,13,23</sup> (Fig.  
95 2a). The density values matched the targets given in the configuration file, the nearest neighbour and  
96 the pairwise distance distribution always exceeded cell diameter, and radial distribution function  
97 demonstrated the homogeneity of cell distribution without overlapping (Fig. S1).

#### 99 3.2.2 Neuron connectivity

100 The network connections summed up to 1'500'000 chemical synapses and 2'100 electrical  
101 synapses. The cerebellar connectome was modelled combining probabilistic and geometric rules that  
102 were chosen depending on available data and the nature of fiber (axon and dendrites) crossing (Fig.  
103 2b,c,d; see Methods for details). This flexible management of connections rules is unique and fixes  
104 problems not easy to solve with cerebral cortex simulators, which deal with isotropic cellular  
105 organizations and adopt a limited number of intersection rules for all neurons and connections<sup>8-10</sup>.

106 The well-known connectivity of *mf* and *glom* was entirely accounted for by literature data. The  
107 BSB generated local anisotropic *glom* clusters extending 60  $\mu\text{m}$  along the *x*-axis and 20  $\mu\text{m}$  along the  
108 *z*-axis<sup>24</sup>, with  $\sim 20$  *gloms* per *mf*<sup>25</sup>. Imposing that each *GrC* sends its 4 dendrites to *gloms* belonging to  
109 different *mfs* within about 30  $\mu\text{m}$ , the BSB yielded 49 *GrCs* per *glom* on average<sup>26,27</sup>. Each of the 4  
110 *GrC* dendrites, in addition to a single excitatory synapse on the terminal compartment, also hosted 1  
111 inhibitory synapse on the preterminal compartment, mostly originating from different *GoCs* (Fig. 2c)  
112 <sup>28,29</sup>.

113 The connectivity of *GoCs* was faced using either literature data (*glom-GoC*) or adopting various  
114 intersection rules (*aa-GoC*, *pf-GoC*, *GoC-GoC*). In fair agreement with literature, each *GoC* received  
115 excitation from 56 different *gloms* and each *glom* collected basolateral dendrites from  $\sim 2$  *GoCs*<sup>30</sup>. There  
116 were 320 *aa* synapses on basolateral dendrites and 910 *pf* synapses on apical dendrites per *GoC*, all  
117 from different *GrCs* (Fig. 2b)<sup>31</sup>. Moreover, each *GoC* received inhibition from 16 other *GoCs*<sup>32</sup> on  
118 basolateral dendrites (subsequent functional calibration implied  $\sim 160$  synapses per pair, see below).  
119 Finally, there were  $\sim 8$  *GoCs* that formed gap junctions on other *GoCs*, with  $\sim 3.5$  gap junctions per pair  
120 <sup>33</sup>.

121 The connectivity of *PCs* and *MLIs* was recovered using suitable intersection rules (*aa-PC*, *pf-*  
122 *PC*, and all *MLI* synapses). The BSB identified 1'500 *pf* synapses per *PC* (this figure was limited by  
123 the 200- $\mu\text{m}$  network size along *z*-axis but it would range up by 1 order of magnitude in an unbounded  
124 volume<sup>18,34,18</sup>) and 197 *aa* synapses per *PC* from 82 different *GrCs*<sup>35</sup>. There were 480 *pf* synapses per  
125 *SC* and 740 *pf* synapses per *BC*, while *MLI* reciprocal inhibition<sup>36</sup> involved 14 *SC-SC* and 14 *BC-BC*  
126 connections with  $\sim 100$  synapses per pair. The *SC* axon, mainly extending on the coronal plane,  
127 innervated  $\sim 2$  *PCs*<sup>37</sup> and each *PC* received synapses from  $\sim 5$  *SCs* (Fig. S2). The *BC* axon, mainly  
128 extending on the sagittal plane, innervated  $\sim 14$  *PCs* and each *PC* received synapses from  $\sim 20$  *BCs* (akin  
129 with the figure of 3-50 baskets around the *PC* soma and 7-10 *PCs* per *BC*)<sup>37,38</sup>. These predictions of  
130 structural parameters were further assessed and tuned through functional simulations (see below).

131

### 132 3.3 Cerebellar network simulations

133 Network simulations were carried out using detailed neuronal and synaptic models written in  
134 NEURON for *GrC*<sup>17</sup>, *GoC*<sup>16</sup>, *PC*,<sup>18</sup> *SC* and *BC*<sup>19</sup>. Local microcircuit responses to input patterns were  
135 tracked back to individual neurons and used to follow signal propagation with unprecedented resolution.  
136 All simulations were carried out in the presence of background noise to improve comparison with  
137 recordings *in vivo*. The emerging spatio-temporal dynamics provided functional model validation  
138 beyond constructive validity based on internal connectivity and single neuron responses (Movie S1).

139

### 140 3.3.1 Resting state activity of the cerebellar network

141 A random input at low frequency (4 Hz Poisson) on all *mfs*<sup>20</sup> was used to simulate the cerebellar  
142 network in resting state *in vivo*. Since anatomical data about the connectivity of cerebellar neurons are  
143 incomplete, but their resting discharge frequency is known, we finetuned the number of connections  
144 per pair against target values of basal discharge. The turning point was to calibrate *GoC-GoC* inhibition,  
145 which influenced resting state activity of the entire network. Since the synaptic conductance (~ 3200  
146 pS) and the number of interconnected *GoCs* (about 15) are known<sup>32</sup>, we tuned the number of *GoC-*  
147 *GoC* synapses until basal discharge frequency was achieved. Eventually, the background frequency of  
148 all cerebellar neuron types fell in the ranges reported *in vivo* in anaesthetized rodents (*mfs*:  $4.2 \pm 2.6$   
149 Hz; *GrCs*:  $0.81 \pm 1.3$  Hz; *GoCs*:  $19 \pm 15$  Hz; *PCs*:  $31 \pm 1.6$  Hz; *BCs*:  $11 \pm 5.1$  Hz; *SCs*:  $9.4 \pm 12$  Hz)  
150 [*GrCs*<sup>39</sup>, *GoCs*,<sup>16,40,41</sup>, *PCs*<sup>42</sup>, *SCs* and *BCs*<sup>43-45</sup>].

151 Background *mf* activity is known to generate synchronous low-frequency oscillations in the  
152 granular layer<sup>46</sup>. Indeed, in the model, the FFT of *GoC* and *GrC* firing revealed a synchronous  
153 oscillatory behaviour in the theta band, with the first harmonic peaking at 9.7 Hz. When *GoC-GoC gap*  
154 junctions were switched off, the regularity of the oscillation decreased and the first FFT harmonic  
155 moved out of theta band (Fig. 3a)<sup>47</sup>.

156

### 157 3.3.2 Impulsive response of the cerebellar network

158 Short stimulus bursts were delivered to a bundle of 4 *mfs* connected to ~80 *gloms* to emulate  
159 whisker/facial sensory stimulation *in vivo*<sup>20,39</sup>. The burst propagated through the network, temporarily  
160 raising neuronal firing (Fig. 3b, Movie S1). The relationship between the number of spikes at afferent  
161 synapses and the response frequency to the *mf* burst was robustly captured by multiple linear regression  
162 (Fig. 3c; Fig. S3a; Fig. S4).

#### 163 3.3.2.1 *GrC* responses

164 Fundamental predictions on how *GrCs* respond to incoming bursts derive from current clamp  
165 recordings *in situ*<sup>48</sup> and simulations<sup>17</sup>, which revealed the role of synaptic receptors and ionic channels.  
166 In BSB simulations, bursts on a collimated *mf* bundle activated a dense cluster of *GrCs*<sup>15,21,49</sup>. The  
167 relationship between the number of input spikes (both at *GoC-GrC* and *glom-GrC* synapses) and *GrC*  
168 response frequency unveiled 4 groups of *GrCs* with a corresponding number of synaptically activated  
169 dendrites (Fig. 3c). The number of *GrC* spikes, first spike latency and dendritic  $[Ca^{2+}]_{in}$  correlated with  
170 the number of active dendrites (NMI = 0.71, 0.86, 0.59, respectively) (Fig. 4a,b).

171 When the inhibitory mechanisms (comprising transient and persistent inhibition) were switched  
172 off to simulate a pharmacological GABA-A receptor blockade, (i) *GrC* baseline frequency increased,  
173 (ii) a tail discharge appeared after the burst, (iii) responses including more spikes appeared, (iv) the first  
174 spike latency decreased, and (v) response variability decreased (Fig. 4a,b). The number of *GrC* spikes,  
175 first spike latency and dendritic  $[Ca^{2+}]_{in}$  still correlated with the number of active dendrites (NMI =

176 0.79, 0.85, 0.61, respectively) (Fig. 4b). Interestingly, inhibition caused a reduction in the number of  
177 active *GrCs* (i.e. those firing  $\geq 1$  spike in the 40 ms after the *mf* burst onset were  $3390 \pm 431$ , and  $8348$   
178  $\pm 1724$  with GABA-A off;  $n=10$  simulations;  $p < 0.001$ , unpaired *t*-test) but enriched the spike pattern,  
179 as predicted theoretically<sup>11,50</sup>.

180 Recordings *in vivo* disclosed precise integration of quanta and high-fidelity transmission in the  
181 granular layer<sup>20,51–54</sup>. In BSB simulations, *GrCs* receiving maximum excitation generated one action  
182 potential for each spike of the input burst, with short latency ( $< 2$  ms), and faithfully followed the input  
183 up to 250 Hz (Fig. 4a) (Movie S2).

#### 184 3.3.2.2 *GoC responses*

185 Following punctuate sensory stimulation *in vivo*, *GoCs* have been reported to respond with  
186 short bursts of 2–3 spikes at up to 200–300 Hz<sup>55</sup>. In BSB simulations, *GoCs* immersed in the *GrC*  
187 active cluster generated a burst of 2-5 spikes with a maximum instantaneous frequency of  $213 \pm 29$  Hz  
188 (Fig. 4c). When GABA synapses and gap junctions between *GoCs* were switched off, the response  
189 bursts showed up to 6 spikes, with a higher maximum instantaneous frequency ( $308 \pm 16$  Hz) ( $n=70$   
190 *GoCs*;  $p < 0.001$ , paired *t*-test) (Fig. 4c). The burst was caused by synaptic excitation relayed by *gloms*  
191 and *GrCs* (through both *aas* and *pfs*), which generated AMPA and NMDA currents in *GoC* dendrites  
192 (Movie S3). The “silent pause” appearing after the burst was caused both by an intrinsic phase-reset  
193 mechanism<sup>55–57</sup> and by reciprocal inhibition between *GoCs*, demonstrating marked dendritic processing  
194 capabilities<sup>16</sup>

#### 195 3.3.2.3 *PC and MLI responses GrCs*

196 *PCs in vivo* are known to respond to punctuate stimulation with burst-pause patterns<sup>22,58</sup>. In  
197 BSB simulations, *PC* responses depended on cell position relative to the *mf* active bundle (Fig. 5a). The  
198 *PCs* placed vertically on top of the *GrC* active cluster received the largest number of *aa* and *pf* synaptic  
199 inputs producing typical burst-pause patterns<sup>18</sup>. The *burst coefficient* was correlated with the number  
200 of synaptic inputs from *pf* and *aa* (multiple regression analysis:  $R^2=0.91$ ) (Fig. 5b). The *pause*  
201 *coefficient* was correlated with the *burst coefficient* (NMI=0.79) and with the number of spikes from  
202 *MLIs* (NMI=0.66) (Fig. 5b), reflecting the origin of the pause from both intrinsic after-hyperpolarizing  
203 mechanisms and *MLI* inhibition<sup>59</sup>. Indeed, *MLIs* are known to narrow the time window and reduce the  
204 intensity of *PC* responses<sup>43</sup>. In BSB simulations, the *PC* AMPA current arose soon after the spikes  
205 emitted by *GrCs*, while the *PC* GABA current was delayed by 2.6 ms (Fig. 5c). In summary, the di-  
206 synaptic IPSCs produced by *MLIs* quickly counteracted the monosynaptic EPSCs produced by *aas* and  
207 *pfs*, providing precise time control over *PC* activation<sup>49,60</sup>.

208 *BCs in vivo* are known to generate lateral inhibition reducing *PC* discharge below baseline  
209 causing contrast enhancement<sup>43,50</sup>. In BSB simulations, this pattern emerged during stimulation of a *mf*  
210 bundle (100 ms @ 50 Hz stimulation on 24 neighboring *mfs*). The *PCs* placed in a band 150-200  $\mu\text{m}$   
211 beside the active cluster along the *x*-axis were inhibited, bringing their frequency below baseline. When

212 *MLI-PC* synapses were switched off, the effect disappeared revealing contrast enhancement due to  
213 lateral inhibition (Fig. 5d).

214 The response of *MLIs in vivo* is only partially known<sup>50</sup>. In BSB simulations, *SCs* and *BCs*  
215 intersected by active *pfs* responded to input bursts and their activity remained higher than baseline for  
216 several hundreds of milliseconds, especially in *SCs*<sup>19</sup> (Fig. S3b).

217

218

## 219 4 Discussion

220 This work shows the first detailed model reconstruction and simulations of the cerebellar cortical  
221 network and predicts neuronal activities involved in the propagation of mossy fiber input signals from  
222 the granular to the PC and molecular layer. By means of the BSB model, we have combined  
223 heterogenous data using suitable placement and connectivity rules with accurate multi-compartmental  
224 neuron models. In the optimization process, the model extracted information from the interdependence  
225 of parameters, bound at high-level through ensuing network dynamics, allowing us to fill gaps in  
226 knowledge through constructive rules. In the validation process, the model demonstrated its  
227 compatibility with a wealth of experimental literature data collected over the last decades.

228

### 229 4.1.1 A model-based ground-truth for the cerebellar cortical network

230

231 The statistical and geometrical rules derived from anatomical and physiological works<sup>12,25</sup>  
232 almost completely anticipated network connectivity at the cerebellar input stage. In the BSB model,  
233 each *glom* hosted ~50 excitatory and ~50 inhibitory synapses on as many *GrC* dendrites, plus ~2  
234 excitatory synapse on basolateral dendrites of as many *GoCs*, summing up to ~102 synapses per *glom*,  
235 in agreement with the anatomical upper limit of ~200<sup>28</sup>. Each one of the 4 *GrC* dendrites received an  
236 excitatory and (in most cases) an inhibitory input from as many different *mfs* and *GoCs*, respectively  
237<sup>29,30</sup>. Each *GoC* received ~320 *aa* synapses on basolateral dendrites and ~910 *pf* synapses on apical  
238 dendrites, according to the figure of ~400 and ~1200<sup>31</sup>, and there were ~3 electrical synapses per *GoC*-  
239 *GoC* pair<sup>47</sup>. Only the number of *GoC-GoC* GABAergic synapses, which amounted to a figure of 160  
240 after functional tuning, lacked an experimental counterpart. In the molecular layer, under geometric and  
241 functional constraints, the BSB model placed limits to the debated numbers determining *PC* and *MLI*  
242 connectivity. The model predicted that ~25% of *aas* contacted the distal dendrites of the overlaying  
243 *PCs* (7·133 out of 28·615 *GrCs*), each *aa* forming 2.4 synapses on average, supporting the important  
244 role predicted for the *aa*<sup>60,61</sup>, while *pfs* formed 1 synapse per *PC* dendritic intersection. In summary,  
245 each *PC* received 12% of the whole *GrC* inputs from *aas*, matching the empirical estimate of 7-24%<sup>62</sup>.  
246 The BSB generated ~25 *SC-PC* and *BC-PC* synapses altogether, which compares well with the  
247 experimental estimate of ~20<sup>63</sup>. Moreover, there were ~17·600 *pf-MLI-PC* synapses (~2·600 *pf-SC-*

248 *PC* and  $\sim 15\,000$  *pf-BC-PC* synapses), compatible with the prediction that the *pf-MLIs-PC* input is  
249 larger than the *pf-PC* input on the same *PC*<sup>64</sup>. In general, since all dendritic trees in the molecular layer  
250 are orthogonal to *pfs*, the BSB reconstruction ranked the number of synapses according to dendritic size  
251 - *PC* ( $\sim 1\,500$ ) > *GoC* ( $\sim 900$ ) > *BC* ( $\sim 700$ ) > *SC* ( $\sim 500$ ) – a figure that would increase proportionately  
252 by scaling the model slab to include full-length *pfs*<sup>65</sup>.

253 Accurate single neuron models with realistic morphology proved also critical to carry out  
254 simulations allowing us to finetune the connectome. In particular, the number of inhibitory synapses  
255 per *GoC-GoC* pair was increased in order to make them fire at  $\sim 19$  Hz [2-30 Hz range<sup>39,55</sup>]. Similarly,  
256 the number of inhibitory synapses per *SC-SC* and per *BC-BC* pairs was tuned in order to make them  
257 fire at  $\sim 10$  Hz [1–35 Hz range<sup>43,44</sup>] and to bring *PCs* into their resting state frequency range of  $\sim 31$  Hz  
258 [ $36.4 \pm 11.5$  Hz<sup>42,66</sup>] *in vivo*.

259 Thus, a reconstruction of model connectivity purely based on geometrical rules was not  
260 sufficient and a careful tuning against functional data was needed. This two-pronged (structural and  
261 functional) approach ensured that all parameters were bound at high-level through the basal neuronal  
262 firing frequency at rest *in vivo*<sup>1</sup>. Eventually, the network connectome is in fair agreement with a wealth  
263 of disparate anatomical and functional determinations, suggesting that the emerging picture provides a  
264 new model-based ground-truth for the cerebellar cortical network.

265

#### 266 4.1.2 Cerebellar network model validation

267

268 The functional validation of single neuron models was previously reported in specific studies  
269<sup>16–19</sup>, so that these neurons could be directly plugged in and used to simulate spatio-temporal network  
270 dynamics *in vivo*. A first validation of the cerebellar network model implied responses to diffused  
271 background noise, which is reported to generate coherent large-scale oscillations<sup>46</sup>. The BSB model  
272 showed indeed that *GrCs* and *GoCs* were entrained into low-frequency coherent oscillations in resting  
273 state and, interestingly, this happened under gap junction control as shown experimentally<sup>47</sup>. A second  
274 functional validation was obtained by simulating responses to naturalistic *mf* bursts, which rapidly  
275 propagated through the *GrC-PC* neuronal chain (Fig. 6) (Movie S1). *GrCs* responded in a dense cluster  
276<sup>49</sup> regulated by *GoCs* and activated soon thereafter the overlaying *PCs* and *MLIs*. In the cluster, 45%  
277 of the *GrCs* fired at least one spike, in agreement with results reported previously<sup>12,49</sup>. Not  
278 unexpectedly, *SCs* and *BCs* effectively reduced activation of *PCs* placed either along or beside the  
279 active *pfs*, respectively, generating feedforward and lateral inhibition<sup>11,12</sup>. *PCs* showed the typical burst-  
280 pause responses that are thought to correlate with cerebellar-dependent behaviors<sup>58</sup>. As a proof of model  
281 sensitivity, these response patterns were seriously altered by changing microscopic parameters, such as  
282 *mf-GrC* neurotransmitter release probability<sup>17</sup>, whose effect propagated from the cerebellar input stage  
283 throughout the whole thickness of the cerebellar cortical network.

284

### 285 4.1.3 Limitations and future challenges

286

287         The most significant problem in this kind of microcircuit models is to incorporate so many  
288 variables that they might be underconstrained. Here we have 5 cell types, 16 synaptic types and as many  
289 ranges for synaptic density. Almost all of them were carefully validated beforehand, except the BC  
290 model with its synapses and the density of reciprocal interneuron inhibitory synapses, which warrants  
291 specific investigation. Thus, although the parameterization of the cerebellar network model relies on  
292 one of the best-defined anatomical and physiological datasets in the brain <sup>12–14,67</sup>, it cannot be excluded  
293 that other parameter combinations might also be effective. Here we have enforced a connectivity  
294 principle largely based on proximity rules between neurites and tuned the connection algorithms to  
295 bring the connectivity within the anatomic-physiological range (see Methods). Alternative algorithms  
296 for automatic parameter tuning may also be used to predict the cerebellar cortical network connectome  
297 <sup>68</sup> and compared to the present results. Finally, while we have used two most representative functional  
298 templates (background oscillations and response to sensory-burst stimulation *in vivo*), others could be  
299 envisaged.

300         Although it is validated on a small network scale (30 k neurons and 1.5 M synapses), the model  
301 is about 1000 times smaller than the whole mouse cerebellum. This would not be a problem if the model  
302 would be a small-scale representation of the cerebellar cortex, but this is not the case given the  
303 anisotropy of cerebellar network architecture. The first issue is that signal propagation along the  
304 transverse plane would require longer modules. Here we have observed the formation of vertical  
305 columns <sup>60,62</sup> but it would be important now to assess <sup>69,70</sup> the beam hypothesis along with spatial signal  
306 filtering and plasticity <sup>11,50,16–19</sup>. Moreover, the cerebellar cortex is subdivided into microzones with  
307 different biochemical and functional properties, while the present model can just be taken as a good  
308 proxy of the Z+ microzone <sup>71–73</sup>. Therefore, the model should be extended and diversified to explore  
309 effects on a larger scale.

310         Another issue is that, in the model, all neurons of the same type are identical one to another.  
311 However, there is morphological and functional variability among neurons of the same type. Moreover,  
312 there are known variants of granule cells, Golgi cells and Purkinje cells <sup>16–18</sup>. It would therefore be  
313 important to explore the impact of neuronal variability, which can bring about relevant computational  
314 effect <sup>74</sup>. The same also applies to synapses, which now have the same release probability and gain at  
315 homologous connections but are tuned by plasticity in real life <sup>16,21,22,34,64,67,72</sup> and could therefore change  
316 network dynamics. The future introduction of plasticity, which now is present only in simplified models  
317 <sup>75,76</sup> and cerebellar subnetworks <sup>11–15</sup>, will allow to refine the effective functional organization of the  
318 connectome and test hypotheses on network functioning.

319         Finally, the operations of the cerebellar cortex are tightly bound to those of the deep cerebellar  
320 nuclei and of the inferior olive. However, to date the only available representations on the mesoscale  
321 are reconstructed using simplified single point neurons <sup>75,76</sup> and a fine grain realistic representation is

322 missing. Therefore, the model could be extended to the mesoscale to investigate how the cerebellar  
323 cortex operates inside the olivo-cerebellar system.

324

#### 325 4.1.4 Conclusions

326

327 In aggregate, the BSB model shows that the geometrical organization of neurites largely  
328 determines cerebellar cortical connectivity and microcircuit dynamics, supporting the original intuition  
329 of J.C. Eccles in the late 60's <sup>11,50</sup>. A similar conclusion was recently reported for the cortical  
330 microcolumn <sup>4</sup>. With appropriate extension, the model could allow to simulate cerebellar modules  
331 including differentiated microzones and microcomplexes <sup>71-73</sup> and more complex patterns of stimuli in  
332 the sensorimotor and cognitive domain <sup>67</sup>. Given the “scaffold” design, new neurons and mechanisms  
333 can be plugged-in to address ontogenesis, species differences (for example in humans) and pathology.  
334 For example, the model may be used to predict the emerging dynamics caused by genetic or epigenetic  
335 alterations in neuron (morphology and function) and synaptic properties, as it is supposed to happen in  
336 ataxia, dystonia and autism <sup>77,78</sup>. The model may also be used to predict the impact of drugs acting on  
337 ionic channels and synaptic receptors. In conclusion, the model can be regarded as a new resource for  
338 investigating the cerebellar network.

339

## 340 5 Materials and Methods

341

### 342 5.1 The BSB modeling framework

343 The BSB is a Python package (RRID:SCR\_008394, version 3.8+) that can be installed on any  
344 device where Python is available (*pip install bsb*) and is open source with source code documentation  
345 and topical tutorials. It includes workflows and building tools for multiscale modeling of networks (both  
346 reconstruction and simulation) and is compatible with a wide variety of target systems such as personal  
347 computers, clusters or supercomputers and provides effortless parallelization using MPI.

348 Although effective tools for microcircuit modeling have recently appeared [BMTK<sup>8,79</sup>, NetPyNE  
349<sup>10</sup>], their connectivity rules deal well with population-level and probabilistic approaches but a subset of  
350 modeling problems remains unsolved, when it comes to dealing with neurons as entities in space with  
351 specific morphologies. The BSB addresses these needs with a set of tools designed to work with  
352 complex network topologies, cell morphologies and many other spatial and *n*-point problems. These  
353 properties allow the BSB to fully empower a “scaffold” modeling strategy, in which a specific brain  
354 region or cell type can be modeled and specific cell placement or connectivity datasets can be changed  
355 without having to regenerate the entire network.

356 There are 3 main phases in the scaffold modeling workflow that can be visited iteratively when  
357 changes need to be made: configuration, reconstruction and simulation. The core concepts of the  
358 framework during the reconstruction phase are i) the network *volume*, with the definition of various  
359 partitions such as layers, meshes or voxel sets (from brain atlases) and arranging elements which can  
360 be structured hierarchically to give rise a complex description of the entire region under consideration,  
361 ii) the *cell types* which determine the properties of cell populations, such as their spatial representation  
362 (soma radius, geometrical extension and/or morphologies) and density information, iii) the *placement*  
363 of said cell types into subspaces of the network volume using certain *placement strategies*, and iv) the  
364 *connectivity* between cell types using certain *connection strategies*. With this information, the  
365 framework places and connects the cells, storing the result in a network reconstruction file. Then the  
366 simulation phase follows, where *cell models*, *synapse models* and *devices* define the simulator-specific  
367 representation of neuron and connection types and input/output variables.

368 All the above concepts (Fig. 1) can be defined in a preceding configuration phase, either in a  
369 configuration file or declared programmatically. The framework was developed with a modular  
370 architecture in mind, where each module revolves around a central polymorphic class: the placement  
371 module has its *PlacementStrategy* and the connectivity module its *ConnectionStrategy*. The users can  
372 provide implementations of any interface to extend the repertoire of default placement or connectivity  
373 strategies with their own. Each user-defined strategy has access to its configuration node, so users can  
374 flexibly configure and parametrize their strategies, leveraging the support provided by the framework.  
375 Various other interfaces exist for less commonly extended functions of the framework, such as

376 configuration parsers (a JSON parser is provided), simulator backends, storage engines (HDF5 and  
377 SONATA backends are provided) or CLI commands.

378 The scaffold builder compiles its models into HDF5 or SONATA files, a format standard for  
379 neural models proposed by the Blue Brain Project and Allen Institute for Brain Science<sup>80</sup>. The HDF5  
380 file is a self-contained hierarchical file that includes all the required information to deploy the model  
381 on another machine, including configuration, placement, connectivity and even morphology  
382 information. These network architecture files can then be used to reproduce results, optimize parameters  
383 or to run entirely different simulations using the same structural information. Parts of the reconstruction  
384 can be repeated independently, and the datasets overwritten or appended with the results. This allows  
385 for quick tentative changes to be made, which improves iteration times of model development, specific  
386 cases and parameter exploration.

387

### 388 5.1.1 Placement

389 The placement is organized into placement objects that consider certain cell types, and a  
390 subspace of the volume. These objects determine the number, position, morphology and orientation of  
391 each cell, according to the desired placement strategy. A variety of configuration mechanisms exist to  
392 define the number of elements to be placed, such as a fixed count, a specific density (volumetric or  
393 planar) or a ratio to the density of another type. Other elements can be instantiated as well, with or  
394 without 3D positions for other purposes (e.g., fibers with their somatic origin outside the considered  
395 brain circuit). A post-processing step after placement may be enabled, where the elements can be  
396 pruned, moved, or labelled (e.g., labelling separate zones with their own connectivity patterns or  
397 identifying individuals to be hubs in a modular network). Each morphology can be rotated based on the  
398 voxel orientation in which it is placed, and fibers crossing multiple voxels can be bent, in order to follow  
399 the surface folding of the region. The main placement strategies are (Fig. 1b):

- 400 - *Particle placement.* The neurons are placed randomly and then checked for collisions, using kd-  
401 tree partitioning of the 3D space<sup>81</sup>. Colliding particles repel each other, the inertia of the particles  
402 is proportional to their radius. It is computationally efficient, yields uniform placement in 3D space,  
403 working properly even in irregular shapes, and it can deal with multiple cell types of different size.  
404 A pruning step can be enabled to remove cells positioned outside the desired subspace.
- 405 - *Parallel array placement.* The neurons are placed in parallel rows on a desired surface, with a  
406 certain angle and specific distances between adjacent cells. A direction-specific jitter can be  
407 configured.
- 408 - *Satellite placement.* The neurons are placed near each cell of an associated type (planet cells).  
409 Satellite positions are chosen at a random distance within a range based on the radii of the planet  
410 cells, so that each planet cell has a certain number of satellite cells around it.

411

412

### 413 5.1.2 Connectivity

414 Each connection identifies a presynaptic element and a postsynaptic element. When multi-  
415 compartmental neuron models are used, the synaptic locations on specific morphology compartments  
416 are also identified. Connections may target either populations, subpopulations, or only specific regions  
417 of the cell morphologies. A post-processing step after connectivity may be enabled, where the identified  
418 synapse locations can be re-distributed (e.g. pruning or moving the synapses). The use of cell  
419 morphologies can be combined with soma-only approaches. Multiple synapses per pair can be  
420 requested, following a probability distribution.

421 The main connectivity strategies provided by the BSB implement different proximity-  
422 probability rules (Fig. 1c):

- 423 - *Touch detection*. The 3D space is partitioned using a kd-tree to search for potentially intersecting  
424 cell pairs. Then, the actual points of intersection are determined using another kd-tree specific to  
425 the pair morphologies, with a maximum intersection distance parameter.
- 426 - *Voxel intersection*. Each presynaptic cell is represented by a voxelized morphology and these voxels  
427 are tested for intersections with the voxels of the postsynaptic cells, using R-tree 3D space  
428 partitioning. When matching voxels are found, random compartments in each voxel are selected,  
429 introducing variability. It is, in this respect, less deterministic than the touch detection strategy<sup>82</sup>. A  
430 *Fiber intersection* variant exists to optimize the case of long, thin neurites, whose path can be  
431 deformed through space according to a 3D field of direction vectors.
- 432 - *Distance-based in/out degree*. A probability distribution is applied to the distance between cells.  
433 Optionally 2 additional probability distributions can be given for the indegree and outdegree  
434 distribution of the network. The number of postsynaptic elements per presynaptic element is  
435 determined by samples of the outdegree distribution. Each postsynaptic target is weighted according  
436 to its distance probability, and the probability to transition from their current indegree  $N$  to indegree  
437  $N+1$ , as dictated by the indegree distribution. To optimize the algorithm, a kd-tree is queried for  
438 cells within a maximum search radius derived from the cumulative probability function of the  
439 distance distribution.

440

### 441 5.1.3 Simulation

442 The BSB can instruct simulators to run the configured models. Although multiple adapters to  
443 different simulators are provided (NEURON - RRID:SCR\_005393; NEST - RRID:SCR\_002963; Arbor  
444 - 10.5281/zenodo.4428108), there is no common high-level language to send instructions across  
445 simulators. Instead, sets of simulator-specific configuration expose the simulator underlying APIs more  
446 directly. These classes contain the simulator-specific logic to fully define inputs, execute, monitor  
447 progress, and collect output of simulations. The interface to the NEURON simulator has been applied  
448 specifically in this work.

449 NEURON<sup>83</sup> cooperates with our Python packages: *Arborize* to create high-level descriptions  
450 of cell models [<https://github.com/dbbs-lab/arborize>], *Patch* to provide a convenience layer on top of  
451 NEURON [<https://github.com/Helveg/patch>], and *Glia* to manage NMODL file dependencies and  
452 versioning [<https://github.com/dbbs-lab/glia>]. Together, these packages and the NEURON adapter  
453 provide out-of-the-box load balanced parallel simulations in NEURON. The adapter is capable of  
454 creating and connecting these *arborized* cell models over multiple cores, implements device models  
455 such as spike generators, voltage and synapse recorders and collects the recorded measurements in an  
456 HDF5 result file. The recorders can specify targets at the cellular or subcellular level, recording  
457 membrane or synapse voltages, conductances, currents and ionic concentrations. These easy  
458 configurable devices allow to monitor all signals propagating across the network to reproduce results  
459 at multiple scales.

460

#### 461 5.1.4 Visualization

462 The BSB provides a plotting module to directly visualize simulation results including 3D network  
463 plots, cell activity in 3D space, PSTH, raster plots, synaptic currents mapped on cell morphologies, and  
464 more. The BSB provides a Blender module containing a complete blender pipeline for rendering videos  
465 of the network activity on a single machine or a cluster. The BSB can be used in Blender Python  
466 environment and provides functions to synchronize the state of the network with the Blender scene, to  
467 animate results or to generate *debug frames*, to troubleshoot placement, connectivity or simulation  
468 issues.

469

## 470 5.2 The cerebellar cortical model

471 Using the BSB, a mouse cerebellar cortical microcircuit was reconstructed and simulated. The  
472 example reported here refers to a volume partitioned into a granular, Purkinje and molecular layer.  
473 Specifically, the volume extended 300  $\mu\text{m}$  along  $x$ , 200  $\mu\text{m}$  along  $z$ , and 295  $\mu\text{m}$  along  $y$  ( $y$  = layer  
474 thickness; 130  $\mu\text{m}$  granular layer, 15  $\mu\text{m}$  Purkinje cell layer, 150  $\mu\text{m}$  molecular layer). In the reference  
475 system,  $x$ - $y$  is the sagittal plane,  $x$ - $z$  the horizontal plane,  $z$ - $y$  the coronal plane. The reconstructed  
476 volume was  $17.7 \cdot 10^{-3} \text{ mm}^3$ . The model was filled with biophysically detailed compartmental neurons  
477 for each cell type. Some structural data and multiple observations from electrical recordings *in vivo* and  
478 *in vitro* were used as constraints in building the model, further experimental measurements were used  
479 for structural and functional validation.

480

### 481 5.2.1 Neuron placement

482 Both the granular layer and the molecular layer were filled using *particle placement*. The  
483 granular layer is made up of densely packed granule cells (*GrC*) and glomeruli (*glom*) intercalated with  
484 Golgi cells (*GoC*). Furthermore, a certain number of mossy fibers (*mf*) was created (without any 3D

485 position), each terminating in about 20 glomeruli. Each *GrC* emits an ascending axon (*aa*) that raises  
486 perpendicularly to the overlying cerebellar surface and reaches the molecular layer bifurcating into two  
487 opposite branches of a parallel fiber (*pf*) elongating on the *z*-axis (major lamellar axis).

488 The molecular layer was divided into a superficial sublayer (2/3 of the thickness) hosting the stellate  
489 cells (*SC*) and a deep sublayer (1/3 of the thickness) hosting the basket cells (*BC*)<sup>23,84</sup>.

490 The Purkinje cells (*PC*) were placed on a horizontal plane (*x-z*) using *parallel array placement*.  
491 *PCs* were placed along parallel lines, with an inclination angle of about 70° with respect to the major  
492 lamellar axis. The dendritic tree of the *PC* is flattened on the sagittal plane and extends for about 150  
493 μm<sup>18</sup>. The parallel arrays were placed at such a distance that the *PC* dendritic trees did not overlap,  
494 while along the major lamellar axis their somata could be packed closely together. For each neuronal  
495 population, the nearest neighbour, the pairwise distance distribution, and the radial distribution function  
496 were computed.

497

## 498 5.2.2 Knowledge base for microcircuit connectivity

499 This chapter summarizes the fundamental knowledge used to reconstruct cerebellar  
500 microcircuit connectivity and highlights which parameters are reported or absent in literature, implying  
501 the different strategies adopted in the BSB.

502 The connectivity of *mfs* and *gloms* is supported by an extended anatomo-physiological analysis  
503 indicating that (i) each *mf* spreads the input signal into a cluster of *gloms*<sup>24</sup>, (ii) each *GrC* sends its 4  
504 dendrites to *gloms* belonging to different *mfs* within about 30 μm<sup>25</sup>, (iii) 1 excitatory synapse is formed  
505 on the terminal compartment of each *GrC* dendrite<sup>26,27</sup>, (iv) 1 excitatory synapse is formed on *GoC*  
506 basolateral dendrites<sup>30</sup>, (v) 1 inhibitory synapse is formed on the preterminal compartment of each *GrC*  
507 dendrite<sup>85</sup>.

508 The connectivity of *GoCs* is also supported by a robust experimental dataset. (i) *GoCs* receive  
509 an undetermined number of excitatory inputs from *mfs* through *gloms*, that in turn host ~2 *GoC*  
510 basolateral dendrites each<sup>30</sup>. (ii) Given that *GoC-GrC* synapses are inside *gloms*, each *GrC* dendrite  
511 receives inhibition from a *GoC* whose axon reaches the *glom* contacting that dendrite<sup>28,29</sup>. (iii) *GoCs*  
512 may receive as many as ~400 *aa* synapses on basolateral dendrites and ~1200 *pf* synapses on apical  
513 dendrites<sup>31</sup>. (iv) *GoCs* make GABAergic synapses onto other *GoCs*<sup>32</sup>, but their number was not  
514 reported. (v) There are 2-4 gap junctions per *GoC* pair<sup>33</sup>. Therefore, geometrical rules were used to  
515 extract the missing parameters.

516 The connectivity of *PCs* can be derived by the axons intercepting their dendritic tree. (i) There  
517 is one single synapse per *pf-PC* crossing. As a whole, the number of *pf-PC* synapses may range up to  
518 ~100'000<sup>34</sup>, many of which would be silent<sup>86</sup>. Based on spines density<sup>87</sup> and the total length of a *PC*  
519 dendritic tree<sup>18</sup>, the number of possible *pf* synapses was estimated to be 15'000-20'000, with a

520 minimum of ~100 synapses needed to generate a simple spike<sup>35</sup>. (ii) The number of *aa-PC* synapses is  
521 not known but there would be multiple synapses per *aa-PC* pair<sup>35</sup>.

522 The connectivity of *MLI* is not completely defined. It is known that (i) *MLIs* receive excitatory  
523 input from *pfs*, (ii) *MLIs* form inhibitory connections with other *MLIs* of the same type<sup>36</sup>, (iii) collaterals  
524 of a *SC* axon mainly extend on the coronal plane, while collaterals of a *BC* axon mainly extend on the  
525 horizontal plane, innervating multiple *PCs*<sup>37</sup>, (iv) each *PC* receives 3-50 baskets around the soma from  
526 as many different *BCs*<sup>38</sup>, while *SC* axons terminate on intermediate *PC* dendritic branches with 0.3-1.6  
527  $\mu\text{m}$  diameter<sup>37,59,61</sup>.

528

### 529 5.2.3 Selection of microcircuit connectivity rules

530 The connectome of the cerebellar network took into consideration 16 connection types  
531 (identified by their source and target neuronal population): *mf-glom*, *glom-GrC*, *glom-GoC*, *GoC-GrC*,  
532 *GoC-GoC*, *GrC(aa)-GoC*, *GrC(aa)-PC*, *GrC(pf)-GoC*, *GrC(pf)-PC*, *GrC(pf)-SC*, *GrC(pf)-BC*, *SC-PC*,  
533 *BC-PC*, *SC-SC*, *BC-BC*, *GoC-GoC*, *GoC-GoC gap junctions*.

534 Glomerular connectivity is a special case since it is largely constrained by prescribed  
535 neuroanatomical and neurophysiological information. Then, since the *glom* did not have a defined  
536 morphological model, they were connected through probability strategies (*distance-based in/out*  
537 *degree*) to identify nearby compartments for synaptic locations on the target cell types, for which a  
538 realistic morphology was used.

539 Specifically, glomerular connectivity was largely based on prescribed anatomo-physiological  
540 rules:

- 541 - *mf-glom*. The *mf* arborization creates anisotropic clusters of glomeruli and clusters originating from  
542 different *mfs* mixed up with each other to some degree<sup>24</sup>. Taking into account short branches since  
543 the small reconstructed volume, a local branching algorithm grouped glomeruli ( $20 \pm 3$  per cluster,  
544 normally distributed) receiving signals from the same *mf* by a distance-based probability rule.
- 545 - *glom-GrC*. For each *GrC*, a pool of nearby *gloms* were selected based on the distance between the  
546 *glom* barycentre and the *GrC* soma center, and a maximum extension of *GrC* dendrites of 30-40  
547  $\mu\text{m}$ <sup>27</sup>. From the pool, 4 *gloms*, each from a different cluster, were randomly sampled and connected  
548 with one of the 4 *GrC* dendrites.
- 549 - *glom-GoC*. For each *glom*, all *GoCs* with their soma at a radial distance less than 50  $\mu\text{m}$   
550 (corresponding to an average extension of *GoC* basolateral dendrites, isotropically in 3D<sup>14,31</sup>) were  
551 connected. The synapse was placed on a basolateral dendrite using an exponential distribution  
552 favouring the compartments closer to the centre of the *glom*.
- 553 - *GoC-GrC*. This connection absorbed the connection *GoC-glom* which was generated using 3D  
554 proximity and a mean divergence (out-degree) of 40; then, each *GoC* synapsed directly on all *GrCs*  
555 that shared those *gloms*.

556 The rest of the cerebellar connectome was reconstructed by applying *voxel* and *fiber*  
557 *intersection*, and *touch detection*. *Voxel intersection* was preferred when 3D morphologies were  
558 intersecting. This strategy, by introducing a cubic convolution and randomization, reduced overfitting  
559 artifacts arising from the intersection of identical morphologies arranged in the quasi-crystalline  
560 cerebellar microcircuit. *Touch detection* and *fiber intersection* were preferred when dealing with 2D  
561 fibers (i.e. *aa* and *pf*), for which the *voxel intersection* would create cubic volumes not representative  
562 of the fibers as line segments. Therefore, for the connections involving *aas* (*GrC(aa)-GoC* and  
563 *GrC(aa)-PC*), *touch detection* was applied with a tolerance distance of 3  $\mu\text{m}$ . For the connections  
564 involving *pfs* (*GrC(pf)-GoC*, *GrC(pf)-PC*, *GrC(pf)-SC*, *GrC(pf)-BC*), *fiber intersection* was applied  
565 with affinity =0.1 and resolution =20  $\mu\text{m}$ . For the other connections, *voxel intersection* was applied:  
566 *GoC-GoC*, *SC-SC*, and *BC-BC* with affinity =0.5; *SC-PC* with affinity =0.1; *BC-PC* with affinity =1,  
567 *GoC-GoC* gap junctions with affinity= 0.2. For chemical synapses, the presynaptic compartment was  
568 always axonal and the postsynaptic compartment was dendritic or somatic (as for the *BC-PC*  
569 connection). For electrical synapses, gap junctions were created between dendrites. Following  
570 biological indications, specific sectors of morphologies were selected as source or target for synaptic  
571 localization, and, for each connected cell pair, the desired number of synapses was defined, eventually  
572 as a normal distribution (mean  $\pm$  sd) (see table in Fig. 2d).

573 Specific sectors of the dendritic trees of *GoC* and *PC* were used as targets for synapse formation.  
574 *GoCs* receive inhibitory and electrical synapses from other *GoCs* as well as *aa* synapses on basolateral  
575 dendrites in the granular layer, while *pf* synapses impinge on apical dendrites in the molecular layer<sup>31</sup>.  
576 *PCs* receive *aa* and *pf* synaptic inputs on different parts of the dendritic tree, and also *SCs* and *BCs*  
577 target different parts of the neuron<sup>59,61</sup>. (i) *GrC(aa)*  $\rightarrow$  *PC* dendrites with diameter < 0.75  $\mu\text{m}$ <sup>18,39</sup>. (ii)  
578 *GrC(pf)*  $\rightarrow$  *PC* dendrites with diameter between 0.75 and 1.6  $\mu\text{m}$ . (iii) *SC*  $\rightarrow$  *PC* dendrites with diameter  
579 between 0.3 and 1.6  $\mu\text{m}$ <sup>37,59,61</sup>. (iv) *BC*  $\rightarrow$  *PC* soma.

580

#### 581 5.2.4 Multi-compartmental neuron models and synaptic models

582 Detailed multi-compartmental models of *GrC*, *GoC*, *PC*, *SC*, *BC* are available, in which dendritic  
583 and axonal processes are endowed with voltage-dependent ionic channels and synaptic receptors. In  
584 each model, cell-specific aspects critical for function are reproduced, e.g., the role of the axon initial  
585 segment, spontaneous firing and burst-pause behaviour. The following receptor-channel models, all  
586 validated against *in vitro* recordings, and generic gap junction models were inserted in the appropriate  
587 neuron compartments:

- 588 - *GrC* synapses<sup>17,88</sup>. *mf-GrC*: AMPA and NMDA receptors; *GoC-GrC*: GABAalpha1/6 receptors.
- 589 - *GoC* synapses<sup>16</sup>. *pf-GoC*: AMPA; *aa-GoC*: AMPA and NMDA; *mf-GoC*: AMPA and NMDA;  
590 *GoC-GoC*: GABAalpha1, gap junctions<sup>33,89</sup>.
- 591 - *PC* (Z+ type) synapses<sup>59</sup>. *pf-PC* and *aa-PC*: AMPA; *SC-PC* and *BC-PC*: GABAalpha1.
- 592 - *SC* and *BC* synapses<sup>19</sup>. *pf-SC* and *pf-BC*: AMPA and NMDA; *SC-SC* and *BC-BC*: GABAalpha1.

593 Chemical neurotransmission was modelled using the Tzodyks and Markram scheme <sup>90,91</sup> for  
594 neurotransmitter release, and receptors kinetic schemes for postsynaptic receptor activation.  
595 Glutamatergic neurotransmission could activate either only AMPA or both AMPA and NMDA  
596 receptors <sup>92</sup>. GABAergic neurotransmission activated GABA-A receptors <sup>93</sup>. A neurotransmitter  
597 impulse was followed by a slow diffusion wave generating both a transient and a sustained component  
598 of the postsynaptic response, as observed experimentally. Parameters describing release probability,  
599 diffusion, ionic receptor mechanisms, vesicle cycling, recovery time constant, electrical conduction  
600 were derived from the corresponding original papers.

601

## 602 5.2.5 Network simulations: stimulation and analysis

603 All simulations used the NEURON adapter of the BSB and were run in parallel through MPI  
604 on the CSCS *Piz Daint* supercomputer, with a time resolution of 0.025 ms. Simulations started with a  
605 5-s stabilization period followed by a 100 ms initialization period, in which random *mf* inputs  
606 desynchronized the network. In all simulations, spikes and voltage traces at soma of all neurons were  
607 recorded. Depending on specific analyses, in some simulations further microscopic variables were  
608 recorded, as explained below. A set of stimulation protocols reproducing specific spatio-temporal  
609 patterns of *mf* activity was used to functionally validate the cerebellar network model; in some cases,  
610 the protocols were repeated using an altered version of the network model in terms of connectome (“by-  
611 lesion” approach), to quantitatively check the relative roles of the connection types.

612

### 613 5.2.5.1 *Diffused background stimulation*

614 The cerebellum *in vivo* is constantly bombarded by a diffused background noise, which  
615 determines the resting state activity of neurons and is thought to entrain the network into coherent low-  
616 frequency oscillations <sup>46,55,56</sup>. Therefore, we first explored the response of the network model to a  
617 random Poisson noise at 4 Hz <sup>20</sup> on all *mfs* for 4 seconds, proving a testbench to validate the structural  
618 and functional network balance.

619 - *Steady state analysis*. We compared basal discharges in the network to those recorded at rest *in*  
620 *vivo*. The mean frequency of each population was computed.

621 - *Oscillatory state analysis*. We investigated the emergence of low-frequency coherent oscillations  
622 in the *GoC* and *GrC* populations. The power spectrum of *GoC* and *GrC* firing activity was  
623 computed by Fast Fourier Transform (FFT), applied to time-binned spike-counts (2.5 ms bins). The  
624 zero-component was cut off and the FFT was smoothed using a Savitzki-Golay filter (6th order  
625 polynomial, window of 51 bins). The same analysis was performed when *GoC-GoC* gap junctions  
626 were blocked, in order to check the role of electrical coupling in oscillatory behaviour of the  
627 granular layer.

628

629 5.2.5.2 *mf burst stimulation*

630 The cerebellum *in vivo* responds with localized burst-burst patterns to facial or whisker sensory  
631 stimulation<sup>20,51</sup>. These bursts are supposed to run on collimated *mf* bundles generating dense response  
632 clusters in the granular layer and thereby activating the neuronal network downstream<sup>21,22,49,88</sup>. To  
633 simulate this functional response, we delivered a *mf* stimulus burst, superimposed on background noise  
634 at 4 Hz, to 4 *mfs* in the center of the horizontal plane, activating about 80 *gloms*. The *mf* burst lasted 20  
635 ms and was made of 5 spikes at fixed time instants (on average 200 Hz, maximum 250 Hz), within  
636 range of *in vivo* patterns<sup>20,39,51</sup>. Ten simulations were run to account for random variability of the  
637 background input and the network responses. Multiple variables over time were recorded: spike times  
638 and membrane voltages of every cell, synaptic currents in the dendrites of some cells, the internal  
639 calcium concentration  $[Ca^{2+}]_{in}$  in the dendrites of all *GrCs* and of some *GoCs*. Further simulations were  
640 carried out using different values of neurotransmitter release probability at the *mf-GrC* synapse (from  
641  $u=0.43$  to  $u=0.1$  and to  $u=0.9$ ).

- 642 - *General analysis of response patterns*. For each neuronal population, a raster plot and a PSTH (peri-  
643 stimulus time histogram) was computed. Each population was described using Multiple Regression  
644 Analysis: the dependent variable was the average firing frequency during 40 ms after the stimulus  
645 onset, over 10 simulations, and the independent variables were the average numbers of spikes  
646 received from each presynaptic population. The linear regression was reported as direction  
647 coefficients and  $R^2$  score.
- 648 - *Analysis of granular layer responses*. For *GrCs* we related the number of dendrites activated by the  
649 *mf* burst with the number of output spikes and the first spike latency. The same protocol was carried  
650 out while switching-off phasic and tonic inhibition from *GoCs* (GABA-A receptor blockade). This  
651 allowed us to investigate excitatory-inhibitory loops in the granular layer, by estimating the  
652 response patterns of *GrCs*, their latencies, and the fraction of *GrCs* activated compared with the  
653 control condition. Furthermore, for each *GrC*, the level of  $[Ca^{2+}]_{in}$  in the dendrites averaged on 500  
654 ms from the *mf* burst was extracted and these  $[Ca^{2+}]_{in}$  values were related to the number of dendrites  
655 activated by the stimulus. The correlation analysis used Normalized Mutual Information (NMI)<sup>94</sup>.
- 656 - *Analysis of PC responses*. The *PC* response was analyzed to evaluate the burst-pause behavior. For  
657 each *PC*, an automatic algorithm extracted any shortening of the inter-spike intervals during the  
658 stimulus window (*burst coeff.*) and any elongation after the stimulus (*pause coeff.*) compared to  
659 baseline. The *burst coeff.* was correlated with the number of excitatory synaptic inputs (from *pfs*  
660 and *aas*) by multiple regression analysis. The *pause coeff.* was correlated with the number of  
661 inhibitory synaptic inputs (from *MLIs*) received during the burst stimulation (20 ms *mf* burst + 20  
662 ms of delayed effects), by calculating the Normalized Mutual Information (NMI). Furthermore, the  
663 relation between the burst and pause coefficients themselves was analysed, by NMI. Further  
664 simulations were run clamping an on-beam *PC* at -70 mV, recording all synaptic currents. All  
665 excitatory synaptic currents (AMPA from *aas* and *pfs*) and all inhibitory synaptic currents (GABA

666 from *SCs* and *BCs*) were summed up, then the cross-correlation among these two rectified and  
667 normalized currents was calculated, to identify the time lag between them.

668 - *Visualization of subcellular variables.* In some cases, ad-hoc computationally expensive recordings  
669 of multiple microscopic variables were performed. In an example focused on a *GoC*, all synaptic  
670 currents (AMPA and NMDA from *gloms* on basolateral dendrites, AMPA and NMDA from *aas* on  
671 basolateral dendrites, AMPA from *pfs* on apical dendrites, GABA from other *GoCs* on basolateral  
672 dendrites), and  $[Ca^{2+}]_{in}$  were recorded and animated (see *Visualization*).

673

#### 674 5.2.5.3 *Lateral Poisson stimulation*

675 The lateral inhibition from *MLIs* to *PCs* comes from activated *MLIs* providing inhibition to off-  
676 beam *PCs*, mainly from *BCs* due to their axon orientation<sup>43</sup>. To simulate this functional response, we  
677 delivered a 50 Hz Poisson distributed stimulus, lasting 100 ms, superimposed on the background noise  
678 (at 4 Hz), on 24 *mfs* on one side of the volume, to monitor the modulation of *MLI* inhibitory effects on  
679 *PCs* at different distances from the active cluster. Two conditions were evaluated: i) control and ii)  
680 *MLIs* disconnected from *PCs*. Ten simulations for each condition were carried out.

681 - *Analysis of PC responses.* For each *PC*, the average Inter-Spike-Interval (ISI) during 200 ms  
682 baseline and the average ISI during the 100-ms stimulus was computed. The relationship between  
683 the distance of a *PC* from the active cluster and its activity modulation (balance between *GrCs*  
684 excitation and *MLIs* inhibition) was investigated in control condition and in the “no *MLI-PC*”  
685 condition.

686

687

688

## 689 6 Code availability

690 The BSB source code is available at <https://github.com/dbbs-lab/bsb>, and can be installed through *pip*  
691 as a Python package available at <https://pypi.org/project/bsb/>. Documentation can be found at  
692 <https://bsb.readthedocs.io/>.

693

## 694 7 References

- 695 1. Arbib, M. A. & Érdi, P. *Precis of neural organization: Structure, function, and dynamics.*  
696 *Behavioral and Brain Sciences* **23**, (MIT Press, 2000).
- 697 2. D’Angelo, E. & Gandini Wheeler-Kingshott, C. Modelling the brain: Elementary components  
698 to explain ensemble functions. *Riv. del nuovo Cim.* **40**, 273–333 (2017).
- 699 3. Amunts, K. *et al.* The Human Brain Project—Synergy between neuroscience, computing,  
700 informatics, and brain-inspired technologies. *PLOS Biol.* **17**, e3000344 (2019).
- 701 4. Markram, H. *et al.* Reconstruction and Simulation of Neocortical Microcircuitry. *Cell* **163**,  
702 456–492 (2015).
- 703 5. Brette, R. *et al.* Simulation of networks of spiking neurons: A review of tools and strategies. *J.*  
704 *Comput. Neurosci.* **23**, 349–398 (2007).
- 705 6. Hines, M. L. & Carnevale, N. T. The NEURON Simulation Environment. *Neural Comput.* **9**,  
706 1179–1209 (1997).
- 707 7. Gewaltig, M.-O. & Diesmann, M. NEST (NEural Simulation Tool). *Scholarpedia* **2**, 1430  
708 (2007).
- 709 8. Dai, K. *et al.* Brain Modeling ToolKit: An open source software suite for multiscale modeling  
710 of brain circuits. *PLoS Comput. Biol.* **16**, e1008386 (2020).
- 711 9. Gratiy, S. L. *et al.* BioNet: A Python interface to NEURON for modeling large-scale networks.  
712 *PLoS One* **13**, 1–18 (2018).
- 713 10. Dura-Bernal, S. *et al.* NetpyNE, a tool for data-driven multiscale modeling of brain circuits.  
714 *Elife* **8**, 1–26 (2019).
- 715 11. Marr, D. A theory of cerebellar cortex. *J. Physiol.* **202**, 437–470 (1969).
- 716 12. D’Angelo, E. *et al.* Modeling the cerebellar microcircuit: New strategies for a long-standing  
717 issue. *Frontiers in Cellular Neuroscience* **10**, 176 (2016).
- 718 13. Casali, S., Marenzi, E., Medini, C., Casellato, C. & D’Angelo, E. Reconstruction and

- 719 Simulation of a Scaffold Model of the Cerebellar Network. *Front. Neuroinform.* **13**, 37 (2019).
- 720 14. Solinas, S., Nieuwenhuis, T. & D'Angelo, E. A realistic large-scale model of the cerebellum granular  
721 layer predicts circuit spatio-temporal filtering properties. *Front. Cell. Neurosci.* **4**, 12 (2010).
- 722 15. Casali, S., Tognolina, M., Gandolfi, D., Mapelli, J. & D'Angelo, E. Cellular-resolution  
723 mapping uncovers spatial adaptive filtering at the rat cerebellum input stage. *Commun. Biol.* **3**,  
724 1–15 (2020).
- 725 16. Masoli, S., Ottaviani, A., Casali, S. & D'Angelo, E. Cerebellar Golgi cell models predict  
726 dendritic processing and mechanisms of synaptic plasticity. *PLoS Comput. Biol.* **16**, e1007937  
727 (2020).
- 728 17. Masoli, S., Tognolina, M., Laforenza, U., Moccia, F. & D'Angelo, E. Parameter tuning  
729 differentiates granule cell subtypes enriching transmission properties at the cerebellum input  
730 stage. *Commun. Biol.* **3**, 1–12 (2020).
- 731 18. Masoli, S. & D'Angelo, E. Synaptic activation of a detailed Purkinje cell model predicts  
732 voltage-dependent control of burst-pause responses in active dendrites. *Front. Cell. Neurosci.*  
733 **11**, 278 (2017).
- 734 19. Rizza, M. *et al.* Stellate cell computational modeling predicts signal filtering in the molecular  
735 layer circuit of cerebellum. *Sci. Rep.* **11**, (2021).
- 736 20. Rancz, E. A. *et al.* High-fidelity transmission of sensory information by single cerebellar  
737 mossy fibre boutons. *Nature* **450**, 1245–1248 (2007).
- 738 21. Roggeri, L., Riviello, B., Rossi, P. & D'Angelo, E. Tactile stimulation evokes long-term  
739 synaptic plasticity in the granular layer of cerebellum. *J. Neurosci.* **28**, 6354–6359 (2008).
- 740 22. Ramakrishnan, K. B., Voges, K., De Propris, L., De Zeeuw, C. I. & D'Angelo, E. Tactile  
741 stimulation evokes long-lasting potentiation of purkinje cell discharge in vivo. *Front. Cell.*  
742 *Neurosci.* **10**, (2016).
- 743 23. Sultan, F. & Bower, J. M. Quantitative golgi study of the rat cerebellar molecular layer  
744 interneurons using principal component analysis. *J. Comp. Neurol.* **393**, 353–373 (1998).
- 745 24. Sultan, F. Distribution of mossy fibre rosettes in the cerebellum of cat and mice: evidence for a  
746 parasagittal organization at the single fibre level. *Eur. J. Neurosci.* **13**, 2123–30 (2001).
- 747 25. Billings, G., Piasini, E., Lőrincz, A., Nusser, Z. & Silver, R. A. Network Structure within the  
748 Cerebellar Input Layer Enables Lossless Sparse Encoding. *Neuron* **83**, 960–974 (2014).
- 749 26. Jakab, R. L. & Hámori, J. Quantitative morphology and synaptology of cerebellar glomeruli in

- 750 the rat. *Anat. Embryol. (Berl)*. **179**, 81–8 (1988).
- 751 27. Houston, C. M. *et al.* Exploring the significance of morphological diversity for cerebellar  
752 granule cell excitability. *Sci. Rep.* **7**, 46147 (2017).
- 753 28. Hamori, J., Jakab, R. L. & Takacs, J. Morphogenetic plasticity of neuronal elements in  
754 cerebellar glomeruli during deafferentation-induced synaptic reorganization. *J. Neural*  
755 *Transplant. Plast.* **6**, 11–20 (1997).
- 756 29. Mapelli, L., Solinas, S. & D'Angelo, E. Integration and regulation of glomerular inhibition in  
757 the cerebellar granular layer circuit. *Front. Cell. Neurosci.* **8**, 55 (2014).
- 758 30. Tabuchi, S., Gilmer, J. I., Purba, K. & Person, A. L. Pathway-specific drive of cerebellar golgi  
759 cells reveals integrative rules of cortical inhibition. *J. Neurosci.* **39**, 1169–1181 (2019).
- 760 31. Cesana, E. *et al.* Granule Cell Ascending Axon Excitatory Synapses onto Golgi Cells  
761 Implement a Potent Feedback Circuit in the Cerebellar Granular Layer. *J. Neurosci.* **33**,  
762 12430–12446 (2013).
- 763 32. Hull, C. & Regehr, W. G. Identification of an Inhibitory Circuit that Regulates Cerebellar  
764 Golgi Cell Activity. *Neuron* **73**, 149–158 (2012).
- 765 33. Szoboszlay, M. *et al.* Functional Properties of Dendritic Gap Junctions in Cerebellar Golgi  
766 Cells. *Neuron* **90**, 1043–1056 (2016).
- 767 34. Hoxha, E., Tempia, F., Lippiello, P. & Miniaci, M. C. Modulation, plasticity and  
768 pathophysiology of the parallel fiber-purkinje cell synapse. *Front. Synaptic Neurosci.* **8**, 1–16  
769 (2016).
- 770 35. Walter, J. T. & Khodakhah, K. The linear computational algorithm of cerebellar Purkinje cells.  
771 *J. Neurosci.* **26**, 12861–12872 (2006).
- 772 36. Kondo, S. & Marty, A. Synaptic currents at individual connections among stellate cells in rat  
773 cerebellar slices. *J. Physiol.* **509** ( Pt 1, 221–32 (1998).
- 774 37. Ango, F. *et al.* Bergmann Glia and the Recognition Molecule CHL1 Organize GABAergic  
775 Axons and Direct Innervation of Purkinje Cell Dendrites. *PLoS Biol.* **6**, e103 (2008).
- 776 38. Blot, A. & Barbour, B. Ultra-rapid axon-axon ephaptic inhibition of cerebellar Purkinje cells  
777 by the pinceau. *Nat. Neurosci.* **17**, 289–295 (2014).
- 778 39. Wilms, C. D. & Häusser, M. Reading out a spatiotemporal population code by imaging  
779 neighbouring parallel fibre axons in vivo. *Nat. Commun.* **6**, 1–9 (2015).
- 780 40. Solinas, S. *et al.* Fast-reset of pacemaking and theta-frequency resonance patterns in cerebellar

- 781 Golgi cells: Simulations of their impact in vivo. *Front. Cell. Neurosci.* **1**, 4 (2007).
- 782 41. Forti, L., Cesana, E., Mapelli, J. & D'Angelo, E. Ionic mechanisms of autorhythmic firing in  
783 rat cerebellar Golgi cells. *J. Physiol.* **574**, 711–729 (2006).
- 784 42. Arancillo, M., White, J. J., Lin, T., Stay, T. L. & Sillitoe, R. V. In vivo analysis of purkinje  
785 cell firing properties during postnatal mouse development. *J. Neurophysiol.* **113**, 578–591  
786 (2015).
- 787 43. Kim, J. & Augustine, G. J. Molecular Layer Interneurons: Key Elements of Cerebellar  
788 Network Computation and Behavior. *Neuroscience* (2020).  
789 doi:10.1016/j.neuroscience.2020.10.008
- 790 44. Jirenhed, D.-A., Bengtsson, F. & Jörntell, H. Parallel fiber and climbing fiber responses in rat  
791 cerebellar cortical neurons in vivo. *Front. Syst. Neurosci.* **7**, 16 (2013).
- 792 45. Barmack, N. H. & Yakhnitsa, V. Functions of interneurons in mouse cerebellum. *J. Neurosci.*  
793 **28**, 1140–1152 (2008).
- 794 46. Hartmann, M. J. & Bower, J. M. Oscillatory activity in the cerebellar hemispheres of  
795 unrestrained rats. *J. Neurophysiol.* **80**, 1598–1604 (1998).
- 796 47. Dugué, G. P. *et al.* Electrical Coupling Mediates Tunable Low-Frequency Oscillations and  
797 Resonance in the Cerebellar Golgi Cell Network. *Neuron* **61**, 126–139 (2009).
- 798 48. D'Angelo, E., De Filippi, G., Rossi, P. & Taglietti, V. Synaptic excitation of individual rat  
799 cerebellar granule cells in situ: evidence for the role of NMDA receptors. *J. Physiol.* **484**, 397–  
800 413 (1995).
- 801 49. Diwakar, S., Lombardo, P., Solinas, S., Naldi, G. & D'Angelo, E. Local field potential  
802 modeling predicts dense activation in cerebellar granule cells clusters under LTP and LTD  
803 control. *PLoS One* **6**, 21928 (2011).
- 804 50. Eccles, J. C., Ito, M. & Szentágothai, J. *The Cerebellum as a Neuronal Machine. The*  
805 *Cerebellum as a Neuronal Machine* (Springer Berlin Heidelberg, 1967). doi:10.1007/978-3-  
806 662-13147-3
- 807 51. Chadderton, P., Margie, T. W. & Häusser, M. Integration of quanta in cerebellar granule cells  
808 during sensory processing. *Nature* **428**, 856–860 (2004).
- 809 52. Arenz, A., Silver, R. A., Schaefer, A. T. & Margie, T. W. The contribution of single synapses  
810 to sensory representation in vivo. *Science (80- )*. **321**, 977–980 (2008).
- 811 53. Powell, K., Mathy, A., Duguid, I. & Häusser, M. Synaptic representation of locomotion in

- 812 single cerebellar granule cells. *Elife* **4**, (2015).
- 813 54. Ishikawa, T., Shimuta, M. & Häuser, M. Multimodal sensory integration in single cerebellar  
814 granule cells in vivo. *Elife* **4**, (2015).
- 815 55. Vos, B. P., Volny-Luraghi, A. & De Schutter, E. Cerebellar Golgi cells in the rat: Receptive  
816 fields and timing of responses to facial stimulation. *Eur. J. Neurosci.* **11**, 2621–2634 (1999).
- 817 56. Solinas, S. M. G., Maex, R. & De Schutter, E. Dendritic amplification of inhibitory  
818 postsynaptic potentials in a model Purkinje cell. *Eur. J. Neurosci.* **23**, 1207–1218 (2006).
- 819 57. Holtzman, T., Rajapaksa, T., Mostofi, A. & Edgley, S. A. Different responses of rat cerebellar  
820 Purkinje cells and Golgi cells evoked by widespread convergent sensory inputs. *J. Physiol.*  
821 **574**, 491–507 (2006).
- 822 58. Herzfeld, D. J., Kojima, Y., Soetedjo, R. & Shadmehr, R. Encoding of action by the Purkinje  
823 cells of the cerebellum. *Nature* **526**, 439–441 (2015).
- 824 59. Masoli, S. *et al.* Single neuron optimization as a basis for accurate biophysical modeling: The  
825 case of cerebellar granule cells. *Front. Cell. Neurosci.* **11**, 71 (2017).
- 826 60. Bower, J. M. & Woolston, D. C. Congruence of spatial organization of tactile projections to  
827 granule cell and Purkinje cell layers of cerebellar hemispheres of the albino rat: vertical  
828 organization of cerebellar cortex. *J. Neurophysiol.* **49**, 745–766 (1983).
- 829 61. Lu, H., Esquivel, A. V. & Bower, J. M. 3D electron microscopic reconstruction of segments of  
830 rat cerebellar Purkinje cell dendrites receiving ascending and parallel fiber granule cell  
831 synaptic inputs. *J. Comp. Neurol.* **514**, 583–594 (2009).
- 832 62. Gundappa-Sulur, G., De Schutter, E. & Bower, J. M. Ascending granule cell axon: An  
833 important component of cerebellar cortical circuitry. *J. Comp. Neurol.* **408**, 580–596 (1999).
- 834 63. Lennon, W., Hecht-nielsen, R. & Yamazaki, T. A spiking network model of cerebellar  
835 Purkinje cells and molecular layer interneurons exhibiting irregular firing. *Front. Comput.*  
836 *Neurosci.* **8**, 1–10 (2014).
- 837 64. Jörntell, H., Bengtsson, F., Schonewille, M. & De Zeeuw, C. I. Cerebellar molecular layer  
838 interneurons - computational properties and roles in learning. *Trends Neurosci.* **33**, 524–535  
839 (2010).
- 840 65. Soha, J. M., Kim, S., Crandall, J. E. & Vogel, M. W. *Rapid Growth of Parallel Fibers in the*  
841 *Cerebella of Normal and Staggerer Mutant Mice.* *J. Comp. Neurol* **389**, (Wiley-Liss, Inc,  
842 1997).

- 843 66. Zhou, H., Voges, K., Lin, Z., Ju, C. & Schonewille, M. Differential Purkinje cell simple spike  
844 activity and pausing behavior related to cerebellar modules. *J. Neurophysiol.* **113**, 2524–2536  
845 (2015).
- 846 67. D’Angelo, E. & Casali, S. Seeking a unified framework for cerebellar function and  
847 dysfunction: from circuit operations to cognition. *Front. Neural Circuits* **6**, 1–23 (2013).
- 848 68. Reimann, M. W., King, J. G., Muller, E. B., Ramaswamy, S. & Markram, H. An algorithm to  
849 predict the connectome of neural microcircuits. *Front. Comput. Neurosci.* **0**, 28 (2015).
- 850 69. Mapelli, J., Gandolfi, D. & D’Angelo, E. High-pass filtering and dynamic gain regulation  
851 enhance vertical bursts transmission along the mossy fiber pathway of cerebellum. *Front. Cell.*  
852 *Neurosci.* **0**, 14 (2010).
- 853 70. Mapelli, J., Gandolfi, D. & D’Angelo, E. Combinatorial Responses Controlled by Synaptic  
854 Inhibition in the Cerebellum Granular Layer. <https://doi.org/10.1152/jn.00642.2009> **103**, 250–  
855 261 (2010).
- 856 71. Apps, R. & Hawkes, R. Cerebellar cortical organization: a one-map hypothesis. *Nat. Rev.*  
857 *Neurosci.* **10**, 670–681 (2009).
- 858 72. Apps, R. *et al.* Cerebellar Modules and Their Role as Operational Cerebellar Processing Units.  
859 *The Cerebellum* **17**, 654–682 (2018).
- 860 73. De Zeeuw, C. I. Bidirectional learning in upbound and downbound microzones of the  
861 cerebellum. *Nat. Rev. Neurosci.* **22**, 92–110 (2021).
- 862 74. K, P. & NN, U. Intrinsic biophysical diversity decorrelates neuronal firing while increasing  
863 information content. *Nat. Neurosci.* **13**, 1276–1282 (2010).
- 864 75. Geminiani, A. *et al.* Complex dynamics in simplified neuronal models: reproducing Golgi cell  
865 electroresponsiveness. *Front. Neuroinform.* **12**, 1–19 (2018).
- 866 76. Geminiani, A., Casellato, C., D’Angelo, E. & Pedrocchi, A. Complex electroresponsive  
867 dynamics in olivocerebellar neurons represented with extended-generalized leaky integrate and  
868 fire models. *Front. Comput. Neurosci.* **13**, (2019).
- 869 77. Huang, M., de Koning, T. J., Tijssen, M. A. J. & Verbeek, D. S. Cross-disease analysis of  
870 depression, ataxia and dystonia highlights a role for synaptic plasticity and the cerebellum in  
871 the pathophysiology of these comorbid diseases. *Biochim. Biophys. Acta - Mol. Basis Dis.*  
872 **1867**, 165976 (2021).
- 873 78. Peter, S. *et al.* Dysfunctional cerebellar Purkinje cells contribute to autism-like behaviour in  
874 Shank2 -deficient mice. *Nat. Commun.* 2016 71 **7**, 1–14 (2016).

- 875 79. Billeh, Y. N. *et al.* Systematic Integration of Structural and Functional Data into Multi-scale  
876 Models of Mouse Primary Visual Cortex. *Neuron* **106**, 388-403.e18 (2020).
- 877 80. Dai, K. *et al.* The SONATA Data Format for Efficient Description of Large-Scale Network  
878 Models. *SSRN Electron. J.* 1–24 (2019). doi:10.2139/ssrn.3387685
- 879 81. Bentley, J. L. Multidimensional binary search trees used for associative searching. *Commun.*  
880 *ACM* **18**, 509–517 (1975).
- 881 82. Nolte, M., Reimann, M. W., King, J. G., Markram, H. & Muller, E. B. Cortical reliability amid  
882 noise and chaos. *Nat. Commun.* **10**, 1–15 (2019).
- 883 83. Hines, M. L. & Carnevale, N. T. Neuron: A Tool for Neuroscientists. *Neurosci.* **7**, 123–135  
884 (2001).
- 885 84. Whitney, E. R., Kemper, T. L., Rosene, D. L., Bauman, M. L. & Blatt, G. J. Density of  
886 cerebellar basket and stellate cells in autism: Evidence for a late developmental loss of  
887 Purkinje cells. *J. Neurosci. Res.* **87**, 2245–2254 (2009).
- 888 85. Mapelli, L., Rossi, P., Nieuwenhuis, T. & D’Angelo, E. Tonic Activation of GABA B Receptors  
889 Reduces Release Probability at Inhibitory Connections in the Cerebellar Glomerulus. *J.*  
890 *Neurophysiol.* **101**, 3089–3099 (2009).
- 891 86. Isope, P. & Barbour, B. Properties of unitary granule cell→Purkinje cell synapses in adult rat  
892 cerebellar slices. *J. Neurosci.* **22**, 9668–9678 (2002).
- 893 87. Parajuli, L. K. & Koike, M. Three-Dimensional Structure of Dendritic Spines Revealed by  
894 Volume Electron Microscopy Techniques. *Front. Neuroanat.* **15**, (2021).
- 895 88. Diwakar, S., Magistretti, J., Goldfarb, M., Naldi, G. & D’Angelo, E. Axonal Na<sup>+</sup> channels  
896 ensure fast spike activation and back-propagation in cerebellar granule cells. *J. Neurophysiol.*  
897 **101**, 519–532 (2009).
- 898 89. Vervaeke, K., Lorincz, A., Nusser, Z. & Silver, R. A. Gap junctions compensate for sublinear  
899 dendritic integration in an inhibitory network. *Science (80-. ).* **335**, 1624–1628 (2012).
- 900 90. Markram, H. & Tsodyks, M. Redistribution of synaptic efficacy between neocortical  
901 pyramidal neurons. *Nature* **382**, 807–810 (1996).
- 902 91. Tsodyks, M. V. & Markram, H. The neural code between neocortical pyramidal neurons  
903 depends on neurotransmitter release probability. *Proc. Natl. Acad. Sci. U. S. A.* **94**, 719–723  
904 (1997).
- 905 92. Nieuwenhuis, T. *et al.* LTP regulates burst initiation and frequency at mossy fiber-granule cell

- 906 synapses of rat cerebellum: experimental observations and theoretical predictions. *J.*  
907 *Neurophysiol.* **95**, 686–99 (2006).
- 908 93. Nieus, T. R., Mapelli, L. & D’Angelo, E. Regulation of output spike patterns by phasic  
909 inhibition in cerebellar granule cells. *Front. Cell. Neurosci.* **8**, 246 (2014).
- 910 94. Laarne, P., Zaidan, M. A. & Nieminen, T. ennemi: Non-linear correlation detection with  
911 mutual information. *SoftwareX* **14**, 100686 (2021).
- 912
- 913

## 914 8 Acknowledgements/funding

915 This research has received funding from the European Union’s Horizon 2020 Framework Program for  
916 Research and Innovation under the Specific Grant Agreement No. 945539 (Human Brain Project SGA3)  
917 and Specific Grant Agreement No. 785907 (Human Brain Project SGA2) and from Centro Fermi project  
918 “Local Neuronal Microcircuits” to ED. Special acknowledgement to EBRAINS and FENIX for  
919 informatic support and infrastructure.

920

## 921 9 Author contribution

922 CC and RDS designed and developed the informatic framework and performed the simulations; RDS  
923 wrote most of the code; AG, SM, MR, AA contributed with essential model components; RDS, CC,  
924 ED analyzed the data, wrote the manuscript, and prepared the figures; CC and ED coordinated the work  
925 and the EBRAINS interaction. ED promoted the project, supported it financially, defined the  
926 physiological aspects and finalized the manuscript.

927

## 928 10 Conflict of interest:

929 The authors declare that the research was conducted in the absence of any commercial or financial  
930 relationships that could be construed as a potential conflict of interest.

931

932

933

934

## 935 11 Figures and legends

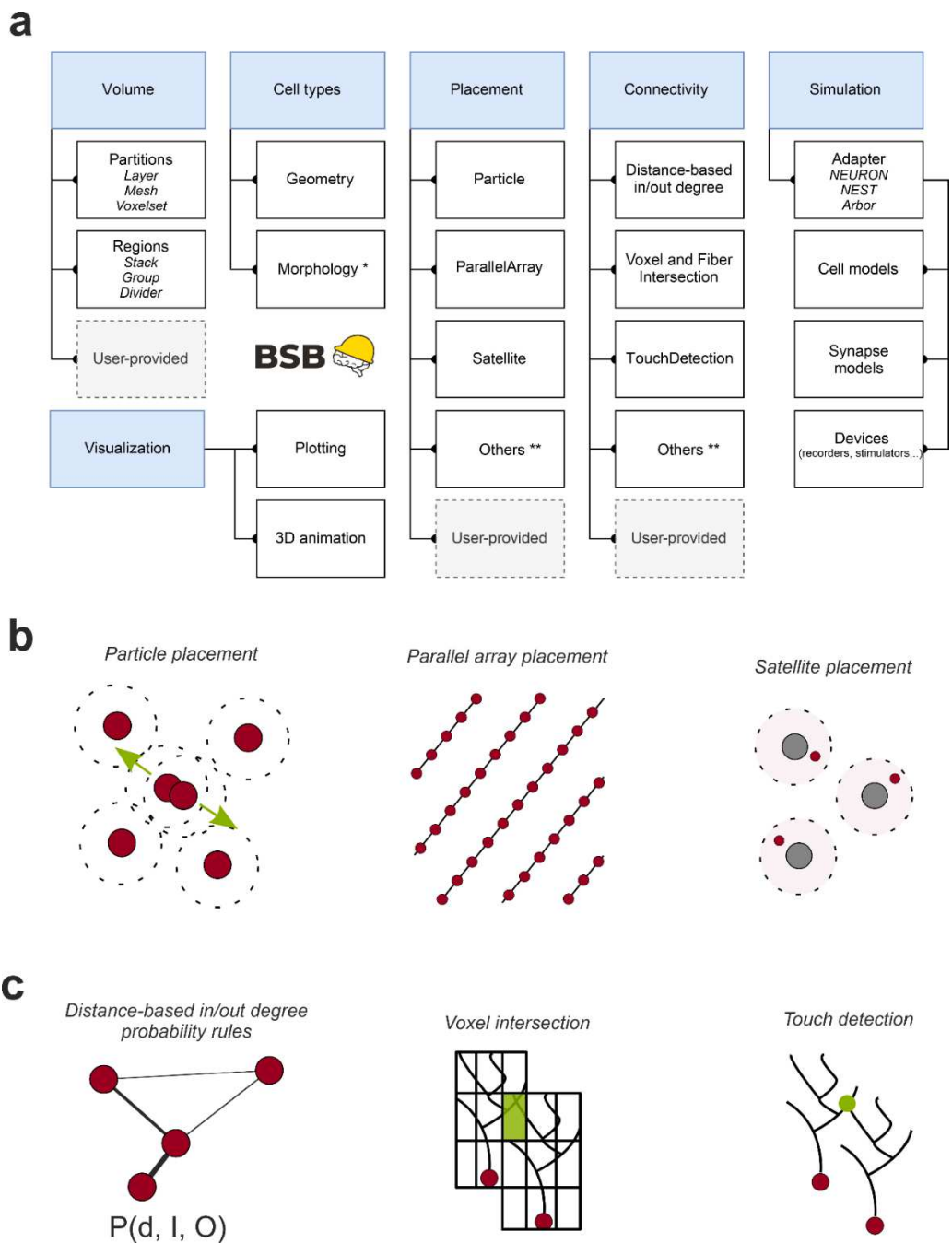
936 Figures, or their specific panels can be visualized as interactive *.html* files from [https://dbbs-](https://dbbs-lab.github.io/deschepper-etal-2021/)  
937 [lab.github.io/deschepper-etal-2021/](https://dbbs-lab.github.io/deschepper-etal-2021/), adding e.g. "figure" + number + panel + ".html" e.g.:  
938 “figure2a.html”, on this URL.

939

940

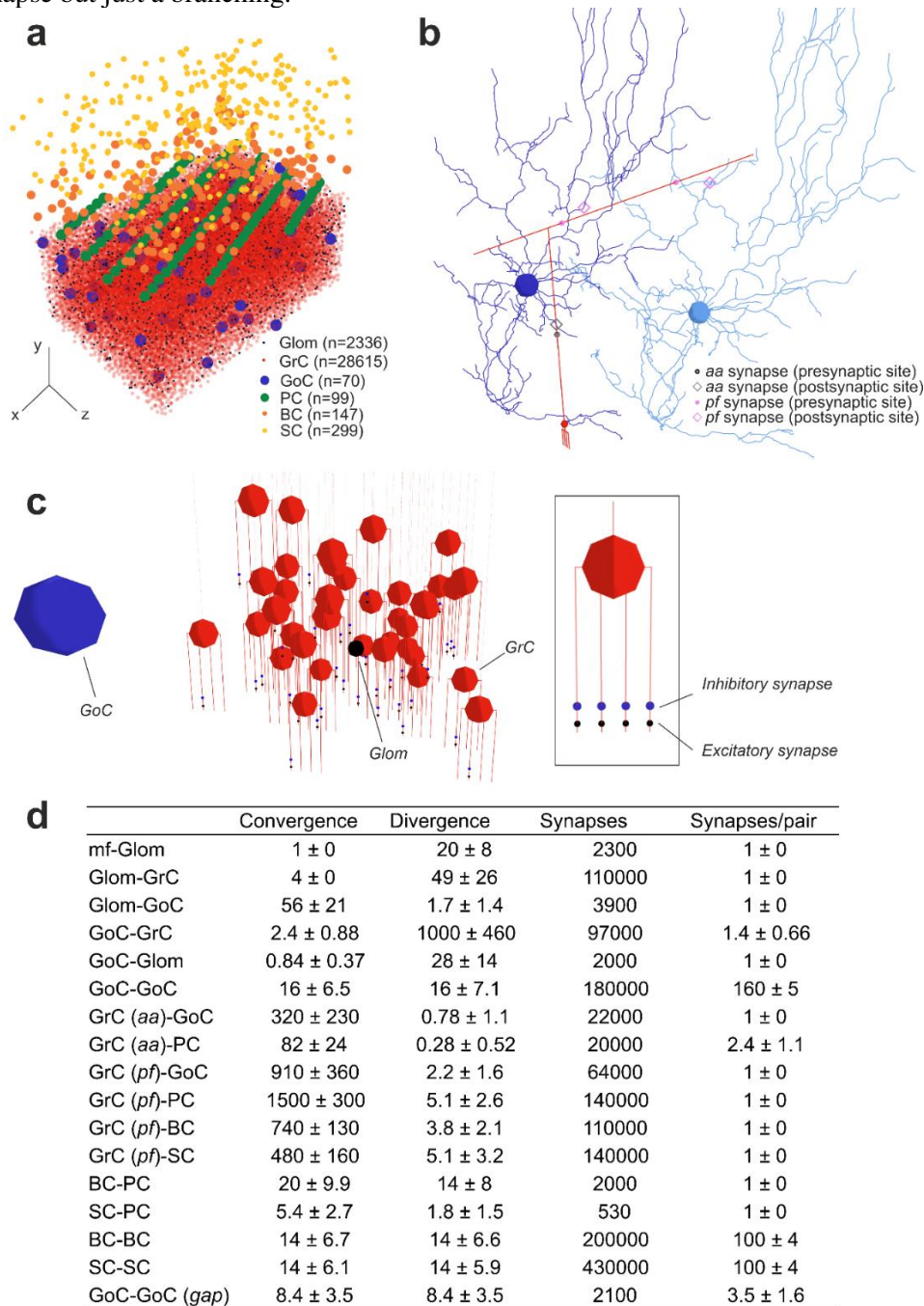
941

942 **Figure 1 | The Brain Scaffold Builder.** (a) Core BSB operations. In the reconstruction phase, BSB  
 943 proceeds by sequentially defining the network *volume*, *cell types*, *cell placement*, *cell connectivity*. Once  
 944 neurons and fibers are positioned, their geometries/morphologies are imported and connection rules  
 945 allow to wire them up and to build the network connectome. In the simulation phase, *neuron* and  
 946 *synapse models* are linked to simulators, like NEURON in the present case, by a specific adapter and  
 947 interfaced to a set of *devices* for stimulation and recording. In the post-simulation phase, graphic tools  
 948 are made available for data representation. This workflow is applicable to any kind of brain neuronal  
 949 network. (b) Infographic representations of the main *placement strategies* available in BSB, using kd-  
 950 tree partitioning of the 3D space (particle placement, parallel array placement, satellite placement). (c)  
 951 Infographic representations of the main *connection strategies* available in BSB: distance-based in/out  
 952 degree probability functions, voxel (or fiber) intersection based on voxelization of morphologies,  
 953 touch detection.



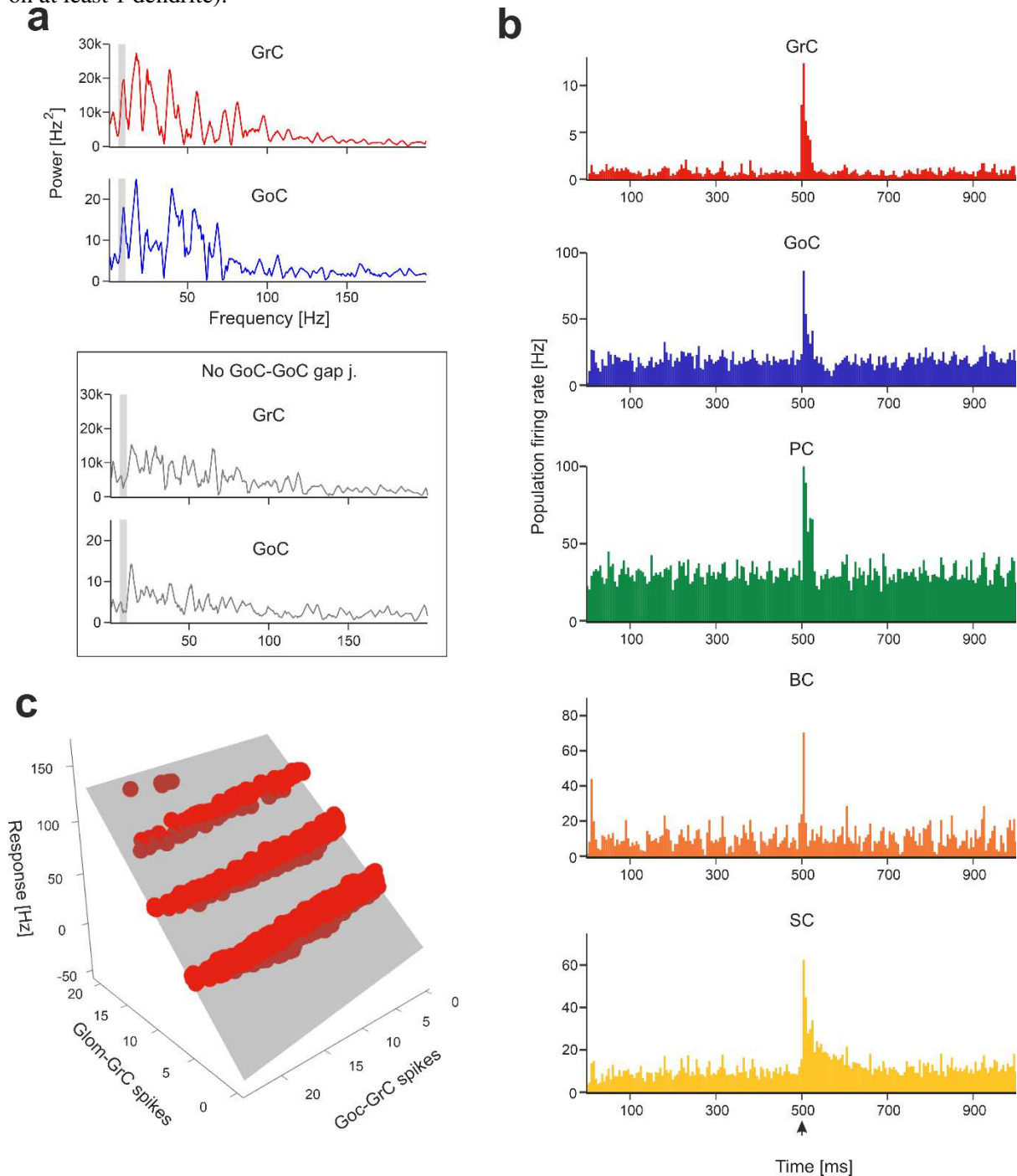
955

956 **Figure 2 | Reconstruction of the microcircuit of cerebellar cortex.** (a) Positioning of cell bodies in  
 957 a 3D slab (300 x 295 x 200  $\mu\text{m}^3$ ) of mouse cerebellar cortex. Cell numbers are indicated (the symbols  
 958 reflect soma size). In this and the following figures, the  $xyz$  reference system is defined by  $x$ - $y$  (sagittal  
 959 plane),  $x$ - $z$  (horizontal plane),  $z$ - $y$  (coronal plane), as in standard anatomical representation. Thus,  $y$   
 960 measures cortex thickness ( $aa$  direction), while  $z$  identifies the major lamellar axis ( $pf$  direction). (b)  
 961 Example of 3D morphologies illustrating  $GrC$ - $GoC$  connections through  $aa$  and  $pf$ . One  $GrC$  and two  
 962  $GoCs$  are shown: the synapse along  $aa$  is identified by *touch detection*, while synapses along  $pf$  are  
 963 identified by *fiber intersection*. (c)  $glom$ - $GrC$  and  $GoC$ - $GrC$  connections. A  $glom$  contacts a group of  
 964 38  $GrCs$  forming an excitatory synapse on the terminal compartment of 1 of their 4 dendrites. The  $glom$ ,  
 965 in turn, is contacted by a  $GoC$  nearby, which forms an inhibitory synapse on the preterminal dendritic  
 966 compartment of the same  $GrCs$ . The inset shows a  $GrC$  with 1 excitatory synapse and 1 inhibitory  
 967 synapse on each dendrite. (d) The cerebellar cortical connectome generated by BSB reporting  
 968 convergence (on the postsynaptic element), divergence (from the presynaptic element), total number of  
 969 synapses, and number of synapses for each connected pair. It should be noted that  $mf$ - $glom$  is not a  
 970 proper synapse but just a branching.



971

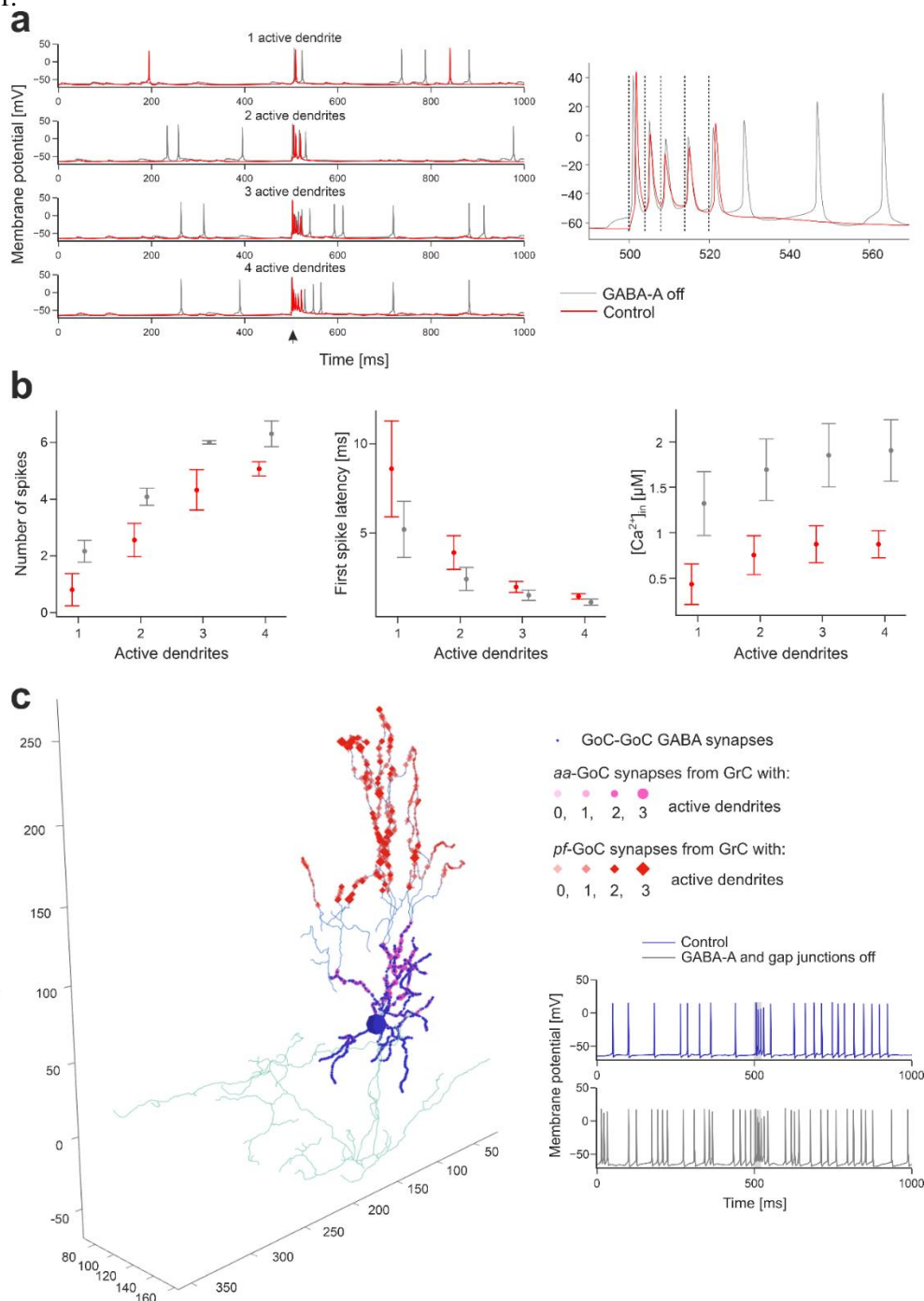
972 **Figure 3 | Network responses to background noise and *mf* bursts.** (a) Power spectra of *GrC* and  
 973 *GoC* activity are computed with Fast Fourier Transform (FFT) of spike time series (total population  
 974 spike-counts in 2.5 ms time-bins). The periodicity of peaks in power spectra reveals synchronous low-  
 975 frequency oscillations in the granular layer. The grey curves represent the power spectra when *GoC*-  
 976 *GoC* gap junctions were disabled, showing a marked decrease in periodicity. The grey bands correspond  
 977 to mouse theta-band (5-10 Hz). (b) The Peri-Stimulus-Time-Histograms (PSTH) of each neuronal  
 978 population show the effect of the localized *mf* burst (onset indicated by arrowhead) emerging over  
 979 background noise. The PSTHs show number of spikes/5 ms time-bins normalized by the number of  
 980 cells, averaged over 10 simulations. (c) Example of multiple linear regression of *GrC* responses (firing  
 981 rate) against the number of synaptic spikes from *gloms* and *GoCs*, during 40 ms after stimulus onset.  
 982 The grey surface is the fitted plane to the points (each point corresponds to a *GrC* receiving the *mf* burst  
 983 on at least 1 dendrite).



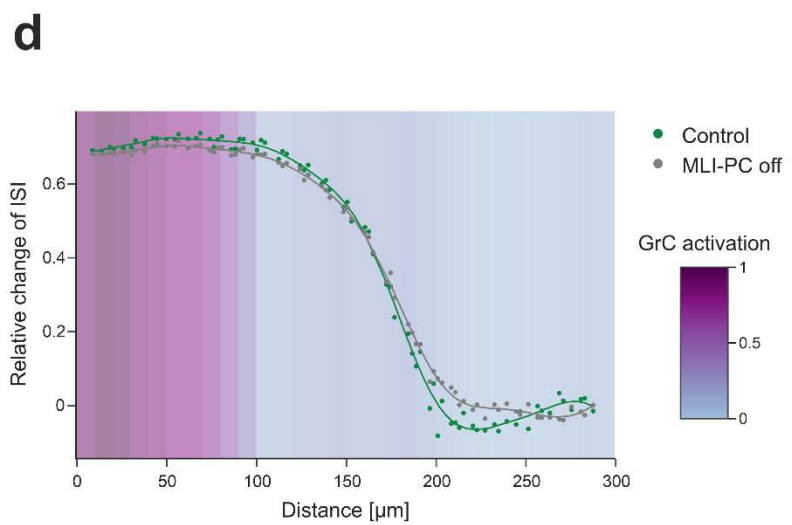
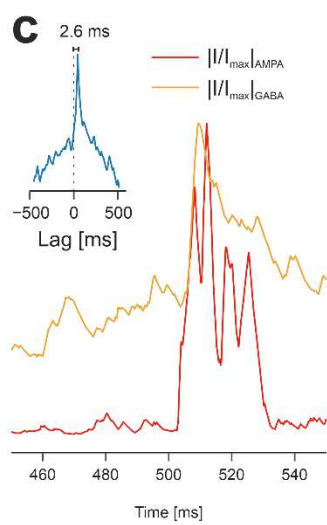
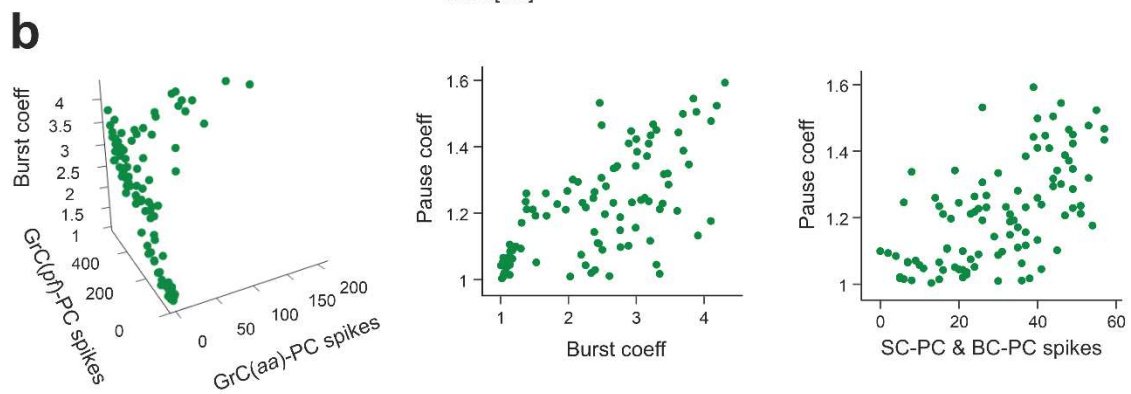
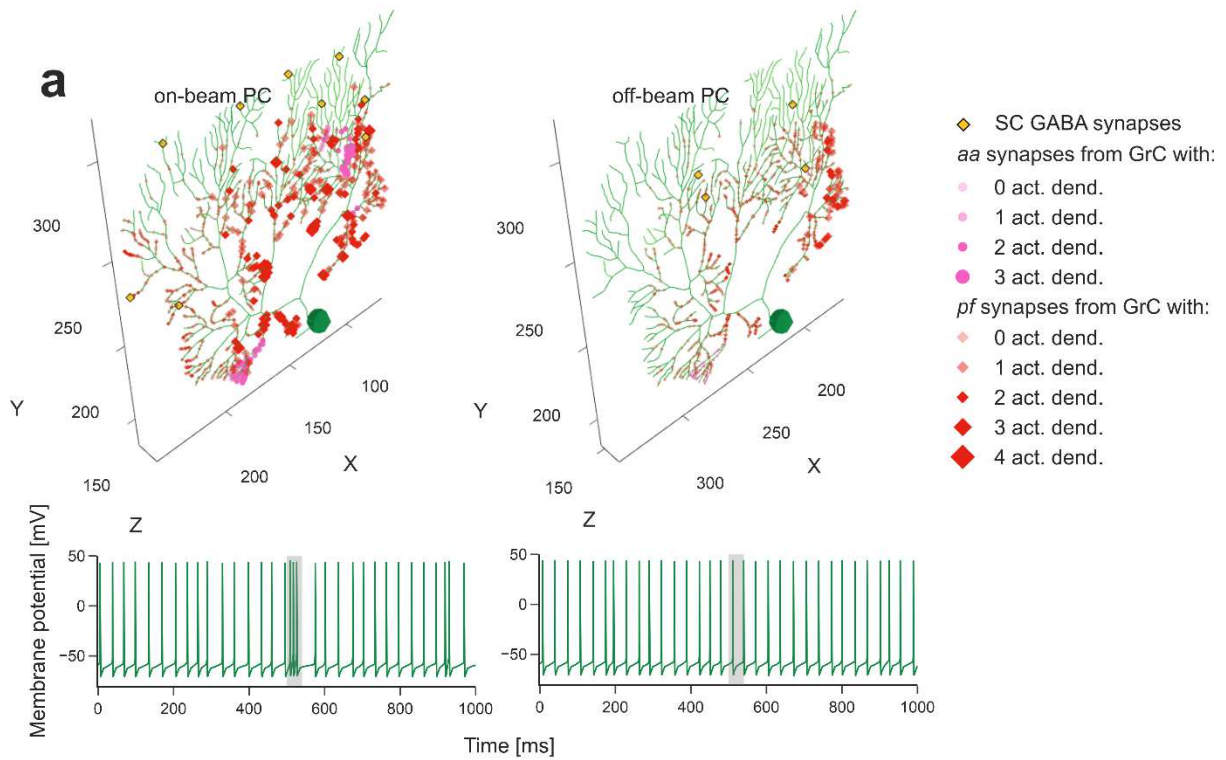
984

985

986 **Figure 4 | Granular layer activation.** (a) Membrane potential of 4 representative *GrCs* with 1 to 4  
 987 dendrites activated by the *mf* burst (20ms@200Hz over background noise, onset indicated by  
 988 arrowhead), in control condition and after GABA-A receptors blockade (“GABA-A off”). The burst  
 989 response of the *GrC* with 4 active dendrites is enlarged on the right to highlight spike-timing (dashed  
 990 lines indicate the *mf* burst spikes). (b) Number of spikes (measured in the 40 ms from *mf* burst onset),  
 991 first spike latency, and dendritic  $[Ca^{2+}]_{in}$  (measured in the 500 ms from *mf* burst onset) in subgroups of  
 992 *GrCs* with the same number of activated dendrites (mean±sd). The graphs compare responses in control  
 993 and during “GABA-A off”. (c) Synapses of a *GoC* activated by *GrCs*. Bigger markers correspond to  
 994 presynaptic *GrCs* more activated by the *mf* burst. The GABAergic synapses from other *GoCs* are on  
 995 basolateral dendrites, *aa* synapses are on basolateral dendrites, *pf* synapses are on apical dendrites. In  
 996 this example, the *GoC* receives 30% of its *aa* synapses and 6% of its *pf* synapses from *GrCs* with at  
 997 least 2 active dendrites. Traces on the right show the *GoC* membrane potential in response to the *mf*  
 998 burst (same stimulation as in (a), grey band) in control and during GABA-A receptors and gap junctions  
 999 switch-off.



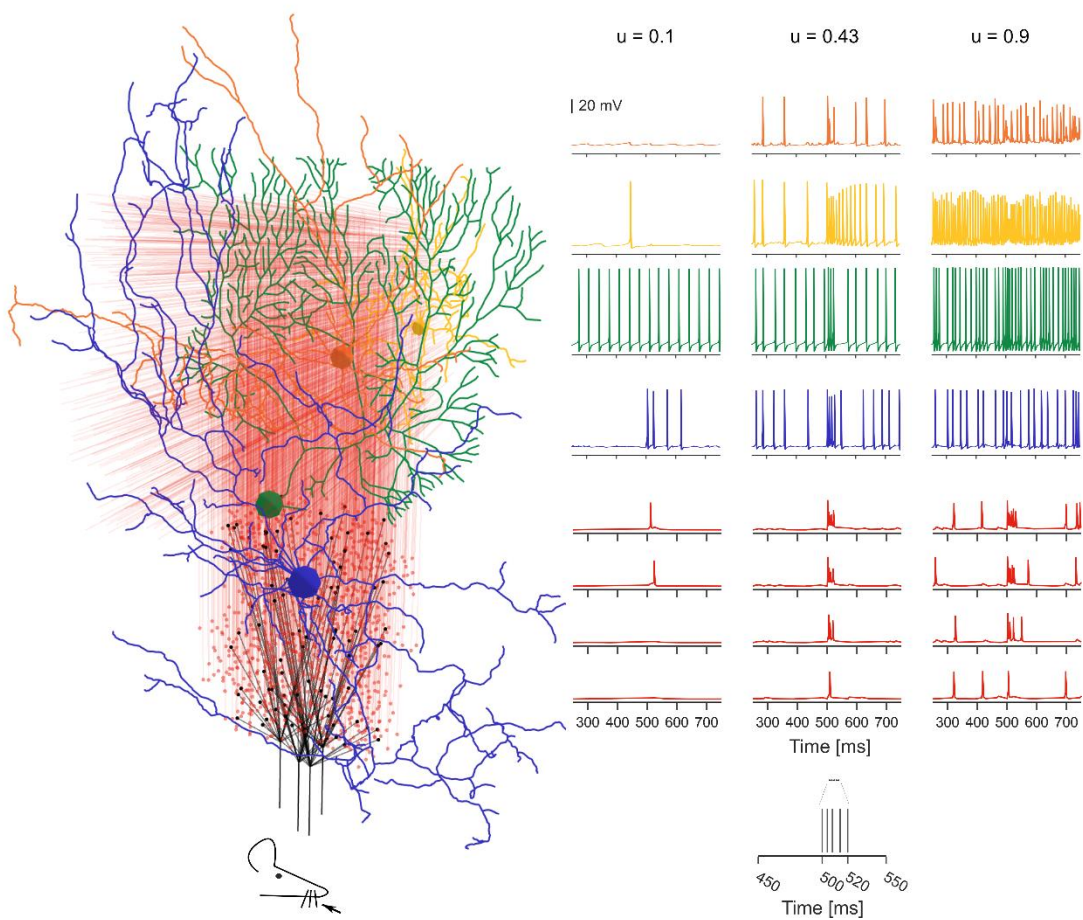
1001 **Figure 5 | Purkinje cell activation.** (a) The *PC* placed on top of the *GrC* active cluster and the *PC*  
1002 placed at its margin show different synaptic inputs. GABAergic synapses from *SCs* are on medium-  
1003 thickness dendrites (those from *BCs* on *PC* soma are not shown), *aa* synapses are located on thin  
1004 dendrites and *pf* synapses on thick dendrites. Bigger markers correspond to presynaptic *GrCs* more  
1005 activated by the *mf* burst. In this example, the on-beam *PC* receives 23% of its *aa* synapses and 6% of  
1006 its *pf* synapses from *GrCs* with at least 2 active dendrites, the off-beam *PC* 0% of its *aa* synapses and  
1007 0.6% of its *pf* synapses from *GrCs* with at least 2 active dendrites. The corresponding membrane  
1008 potential traces are shown at the bottom (the 20ms *mf* burst is highlighted by grey band). (b) Analysis  
1009 of the burst-pause response of *PCs* to the *mf* burst (20ms@200Hz over background noise). The *burst*  
1010 *coefficient* (i.e. the shortening of the inter-spike interval due to the *mf* burst, with respect to baseline) is  
1011 reported against the number of spikes from *aas* and from *pfs* (multivariate regression analysis:  $R^2=0.91$ ).  
1012 The *pause coefficient* (i.e. the elongation of the inter-spike interval after the *mf* burst response, with  
1013 respect to baseline) is reported against either the *burst coefficient* (NMI=0.79) or the number of spikes  
1014 from *SCs* and *BCs* (NMI=0.66). (c) Synaptic currents recorded from the *PC* on top of the *GrC* active  
1015 cluster (same as in (a)), in voltage-clamp. The traces are the sum of all excitatory (AMPA) and inhibitory  
1016 (GABA) dendritic currents during the *mf* burst. They are rectified, normalized and cross-correlated  
1017 (inset) unveiling a GABA current lag of 2.6 ms with respect to AMPA current. (d) By stimulating a *mf*  
1018 bundle (100ms@50 Hz Poisson stimulation on 24 adjacent *mfs*), the *PC* response (modulation with  
1019 respect to baseline) was quantified by the relative change of Inter-Spike-Interval (ISI), during the  
1020 stimulus, where 0 corresponds to baseline. The two series of points compare *PC* response modulation  
1021 when *SCs* and *BCs* were either connected (“control”) or disconnected from *PCs* (“*MLI-PC* off”). The  
1022 curves are regression fittings to the points (Kernel Ridge Regression using a radial basis pairwise  
1023 function, from Python scikit-learn library). The *GrC* active cluster (“*GrC* activation”) was identified by  
1024 a threshold on the stimulation-induced activity by using kernel density estimation.  
1025



1026

1027

1028 **Figure 6 | Activation of a vertical neuronal column in the cerebellar cortex.** A whisker air-puff  
 1029 stimulus (the *mf* burst) is delivered to 4 adjacent *mfs*, which branch in 4 *glom* clusters. *GrCs* respond  
 1030 rapidly with a burst when at least 2 dendrites are activated. A *GrC* dense cluster is formed and the signal  
 1031 propagates up through an *aa* bundle and transversally along a *pf* beam. *GoCs* receive the signal both on  
 1032 basolateral and apical dendrites. *PCs* vertically on top of the active cluster are invested by *aa* and *pf*  
 1033 synaptic inputs. On-beam *SCs* and *BCs* receive signals through *pf* synapses; *SC* axons inhibit mainly  
 1034 on-beam *PCs*, while *BC* axons inhibit mainly off-beam *PCs*. The membrane potential traces (*mf* burst  
 1035 starts at 500 ms) are shown for each neuronal population. Traces in the three columns correspond to  
 1036 three different release probabilities at the *mf-GrC* synapses:  $u=0.1$ ,  $u=0.43$  (control condition used in  
 1037 the rest of the paper),  $u=0.9$ . The lower and higher  $u$ -values are typical of long-term synaptic depression  
 1038 and potentiation in the granular layer.  
 1039



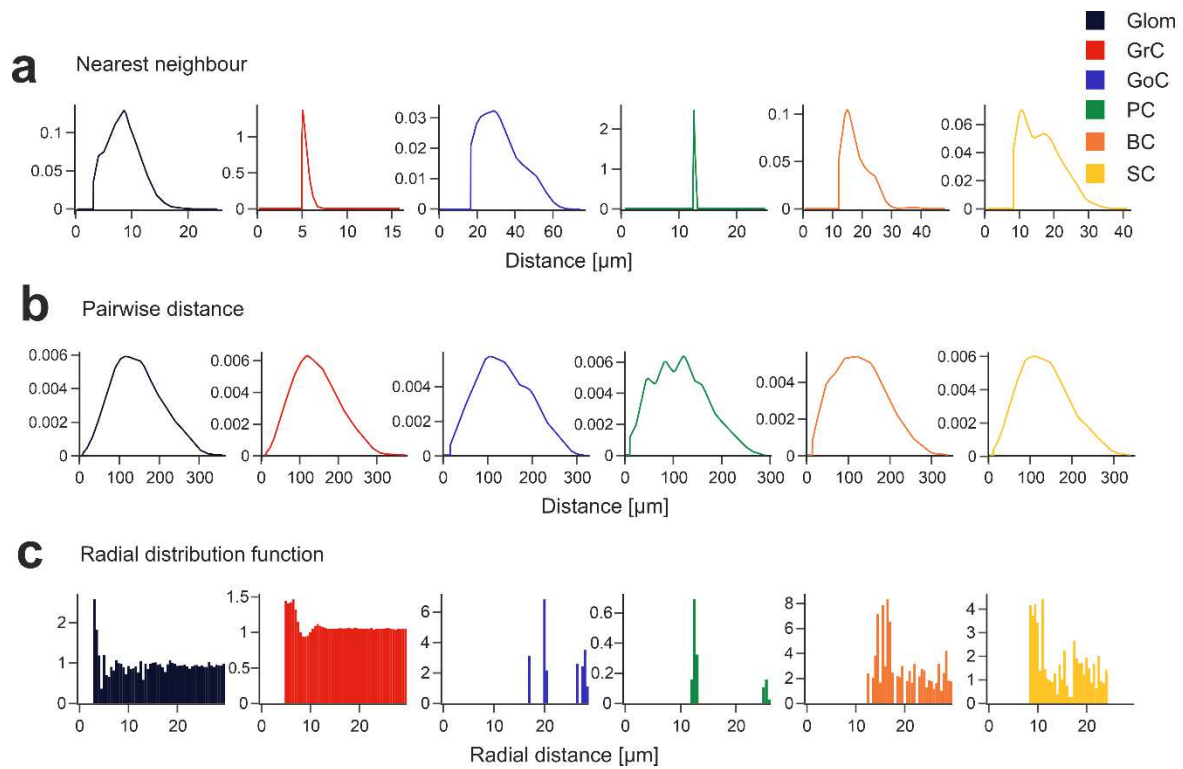
1040

1041

1042 12 Supplementary material

1043 Supplementary figures and videos can be visualized as interactive *.html* files at [https://dbbs-](https://dbbs-lab.github.io/deschepper-et-al-2021/)  
1044 [lab.github.io/deschepper-et-al-2021/](https://dbbs-lab.github.io/deschepper-et-al-2021/), adding e.g. "video" + number + ".html" e.g.: "videoS2.html", on  
1045 this URL.  
1046

1047 **Figure S1 | Placement metrics.** Cell placement is assessed using various metrics for each population,  
1048 including (a) Nearest Neighbor distance, (b) Pairwise Distance, (c) Radial Distribution Function. These  
1049 metrics show realistic cell positioning.  
1050

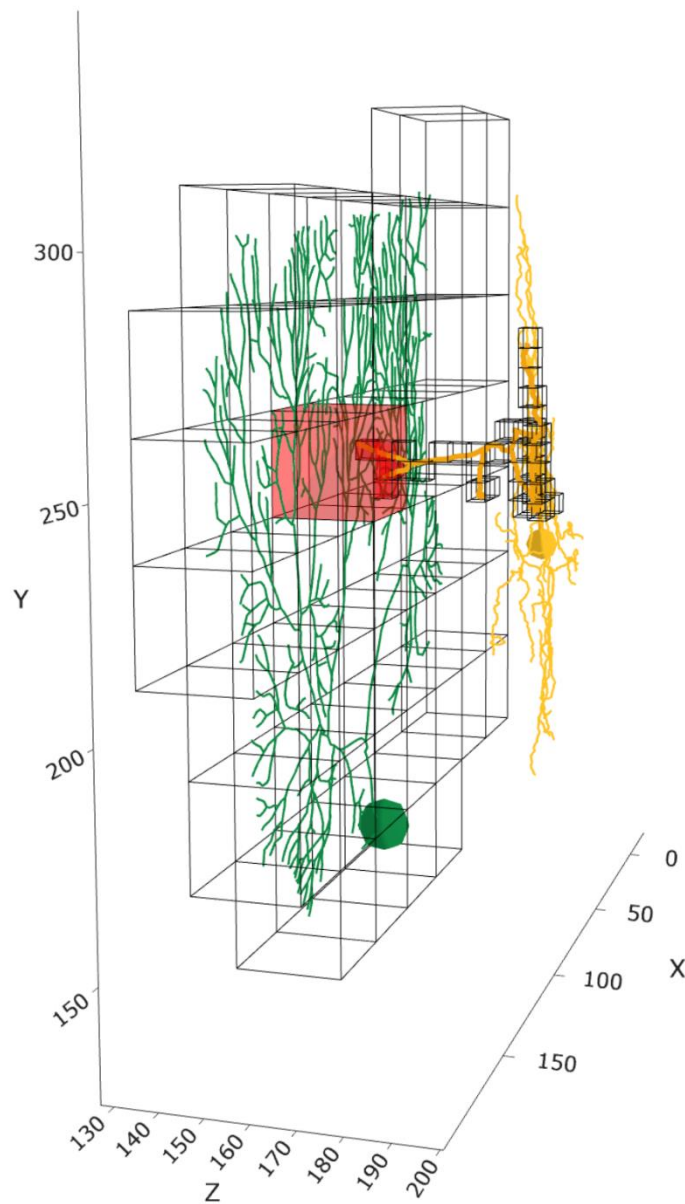


1051

1052

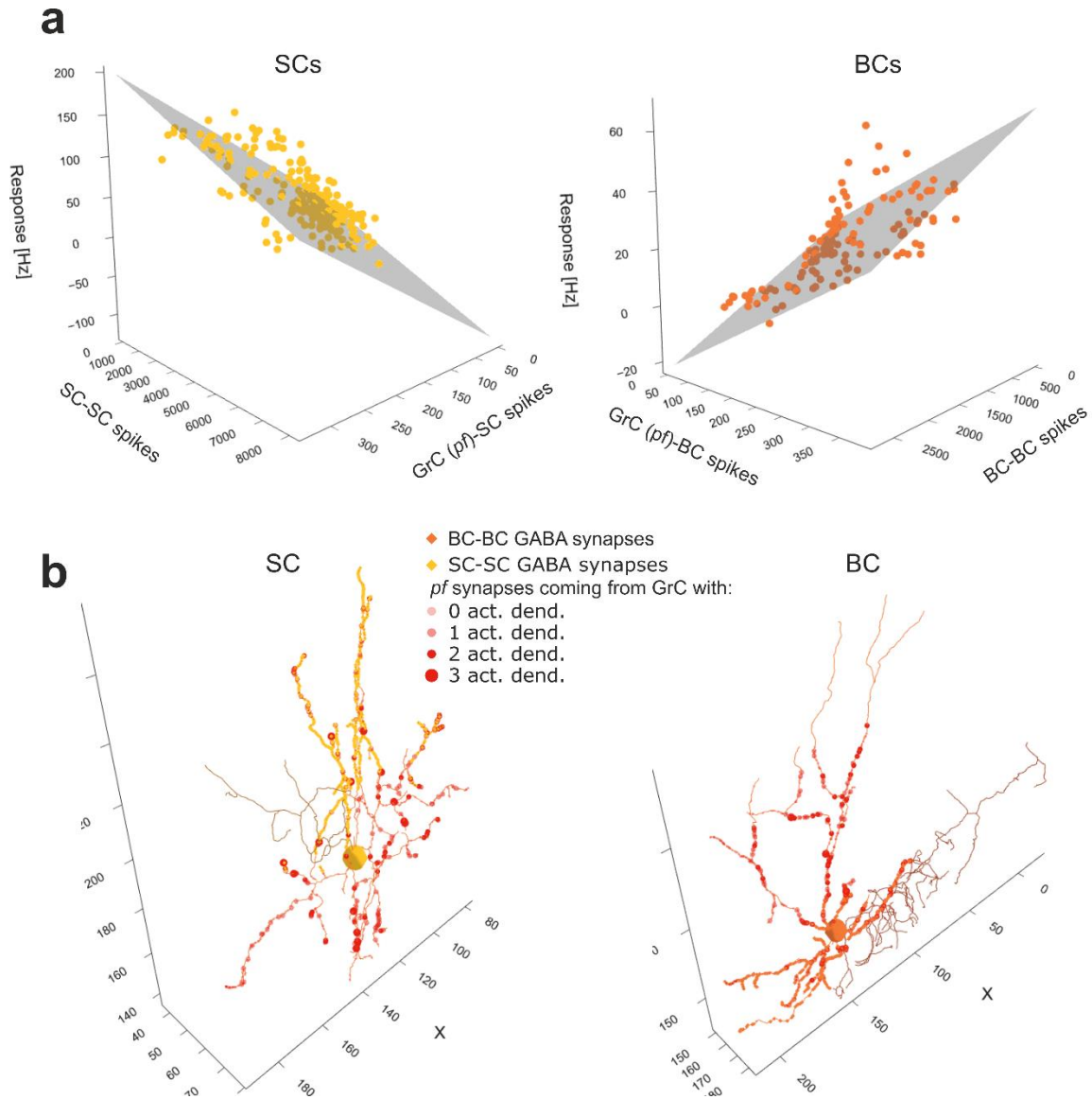
1053

1054 **Figure S2 | Connecting SC-PC by voxel intersection.** A mesh of adjacent voxels is used to enwrap  
1055 the axon of a stellate cell (50 cubes with 4.6  $\mu\text{m}$  side) and the dendritic tree of a PC (50 cubes with 26  
1056  $\mu\text{m}$  side). The intersecting voxels are in red. The synapses are located on compartments within the  
1057 intersecting voxels.



1058  
1059

1060 **Figure S3 | MLI responses to *mf* burst.** (a) Multiple linear regression of SCs and BCs in responses to  
 1061 the *mf* burst against the number of synaptic spikes from *pf*s and from other SCs or BCs. (b) One SC and  
 1062 one BC crossed by an active *pf* beam are represented in 3D. The GABAergic synapses from other SCs  
 1063 or BCs are also indicated. Bigger markers correspond to presynaptic GrCs more activated by the *mf*  
 1064 burst. In this example, the SC receives 8% and the BC 7.5 % of their *pf* synapses from GrCs with at  
 1065 least 2 active dendrites.  
 1066



1067  
 1068

1069 **Figure S4 | Input-output dependency of model neurons.** Multiple linear regression between neuronal  
 1070 responses (firing rates) to the *mf* burst and the number of incoming spikes from the presynaptic neurons  
 1071 (during 40 ms from the *mf* burst onset), averaged over 10 simulations.  $R^2$  and direction coefficients are  
 1072 reported.  
 1073

	$R^2$		Coefficient
GrC	0.91	Glom	6
		GoC	-0.55
GoC	0.81	Glom	0.14
		GrC (aa)	0.15
		GrC (pf)	0.1
		GoC	-0.006
PC	0.95	GrC (aa)	0.057
		GrC (pf)	0.091
		SC	0.074
		BC	-0.2
SC	0.79	GrC (pf)	0.54
		SC	-0.018
BC	0.72	GrC (pf)	0.11
		BC	-0.017

1074  
 1075  
 1076

1077 **Movie S1. Impulsive response of the cerebellar network.** The movie shows the activation of the  
1078 cerebellar network receiving (at movie time = 12 s, indicated by a green light) the *mf* burst (20ms@200  
1079 Hz on a bundle of adjacent 4 *mfs*) to emulate whisker/ facial sensory stimulation *in vivo*, superimposed  
1080 on diffused background noise<sup>20</sup>. Note the sparse activity in *GrCs* that suddenly aggregates into dense  
1081 clusters activating the overlaying *PCs* and *MLIs*. This pattern gives rise to a vertical column of activity  
1082 in the cerebellar cortex (see also Fig.6). It should be noted that, compared to<sup>14</sup>, the granular layer  
1083 occasionally activates clusters of *GrCs* under background bombardment due to the *mf-glom*  
1084 ramifications and clustering that privileges the areas where *gloms* originating from the same *mfs*  
1085 overlap. Nonetheless, this activity is rarely strong enough to cause a visible activation of the overlaying  
1086 *PCs* and *MLIs*.

1087  
1088 **Movie S2. *GrC* response.** The electrical activity of a *GrC* embedded into the cerebellar network (same  
1089 cell as in Fig. 4a with “4 active dendrites”) is animated along with dynamic changes in molecular and  
1090 synaptic variables. The movie shows 100 ms of simulation, with the *mf* burst (20ms@200 Hz on a  
1091 bundle of adjacent 4 *mfs* superimposed on diffused background noise) starting at movie time = 5 s  
1092 (indicated by a green light). Each variable is reported on the *GrC* morphology (4 dendritic  
1093 compartments, soma, axon hillock, ascending axon, parallel fiber) using a colour scale. (**V<sub>m</sub>**) membrane  
1094 potential; (**Ca**) intracellular calcium concentration; (**AMPA**), (**NMDA**) and (**GABA**), synaptic currents  
1095 recorded in voltage-clamp.

1096  
1097 **Movie S3. *GoC* response.** The electrical activity of a *GoC* embedded into the cerebellar network (same  
1098 cell as in Fig. 4c) is animated along with dynamic changes in molecular and synaptic variables. The  
1099 movie shows 100 ms of simulation, with the *mf* burst (20ms@200 Hz on a bundle of adjacent 4 *mfs*  
1100 superimposed on diffused background noise) starting at movie time = 0 s (indicated by a green  
1101 light). Each variable is reported on the *GoC* morphology (using a colour scale) and shown at the bottom  
1102 with traces (using a moving time window) referring to specific neuron compartments: the soma (teal),  
1103 an apical dendrite (pink) and a basolateral dendrite (gold). (**V<sub>m</sub>**) membrane potential traces in the soma  
1104 and apical dendrite. (**Ca**) [Ca<sup>2+</sup>]<sub>in</sub> in the basolateral and apical dendrite. (**AMPA**) synaptic current in the  
1105 basolateral and apical dendrite (synapses from *mfs*, *aas*, and *pfs*). (**NMDA**) synaptic current in the  
1106 basolateral dendrite (synapses from *mfs* and *aas*). (**GABA**) synaptic current in the basolateral dendrite  
1107 (synapses from *GoCs*).

## Supplementary Files

This is a list of supplementary files associated with this preprint. Click to download.

- [movieS2networkActivity.mp4](#)
- [movieS3GrC.mp4](#)
- [movieS4GoC.mp4](#)